*Article*

# Halogens in Eclogite Facies Minerals from the Western Gneiss Region, Norway

**Lewis Hughes [1,*], Simon Cuthbert [2], Alex Quas-Cohen [1], Lorraine Ruzié-Hamilton [1], Alison Pawley [1], Giles Droop [1], Ian Lyon [1], Romain Tartèse [1] and Ray Burgess [1]**

[1] Department of Earth and Environmental Sciences, University of Manchester, Manchester M13 9PL, UK; alexandra.quas-cohen@postgrad.manchester.ac.uk (A.Q.-C.); lorraine.ruzie@manchester.ac.uk (L.R.-H.); alison.pawley@manchester.ac.uk (A.P.); giles.droop@gmail.com (G.D.); Ian.Lyon@manchester.ac.uk (I.L.); romain.tartese@manchester.ac.uk (R.T.); ray.burgess@manchester.ac.uk (R.B.)

[2] Department of Mineralogy, Petrography and Geochemistry, Faculty of Geology, Geophysics and Environmental Protection, AGH University of Science and Technology, al. Mickiewicza 30, 30-059 Krakow, Poland; simon.cuthbert@agh.edu.pl

* Correspondence: lewis.hughes@manchester.ac.uk

**Abstract:** Ultra-high-pressure (UHP) eclogites and ultramafites and associated fluid inclusions from the Western Gneiss Region, Norwegian Caledonides, have been analysed for F, Cl, Br and I using electron-probe micro-analysis, time-of-flight secondary ion mass spectrometry and neutron-irradiated noble gas mass spectrometry. Textures of multi-phase and fluid inclusions in the cores of silicate grains indicate formation during growth of the host crystal at UHP. Halogens are predominantly hosted by fluid inclusions with a minor component from mineral inclusions such as biotite, phengite, amphibole and apatite. The reconstructed fluid composition contains between 11.3 and 12.1 wt% Cl, 870 and 8900 ppm Br and 6 and 169 ppm I. F/Cl ratios indicate efficient fractionation of F from Cl by hydrous mineral crystallisation. Heavy halogen ratios are higher than modern seawater by up to two orders of magnitude for Br/Cl and up to three orders of magnitude for I/Cl. No correlation exists between Cl and Br or I, while Br and I show good correlation, suggesting that Cl behaved differently to Br and I during subduction. Evolution to higher Br/Cl ratios is similar to trends defined by eclogitic hydration reactions and seawater evaporation, indicating preferential removal of Cl from the fluid during UHP metamorphism. This study, by analogy, offers a field model for an alternative source (continental crust) and mechanism (metasomatism by partial melts or supercritical fluids) by which halogens may be transferred to and stored in the sub-continental lithospheric mantle during transient subduction of a continental margin.

**Keywords:** halogens; subduction; metasomatism; eclogite; Western Gneiss Region

## 1. Introduction

Halogens show a range from moderate to highly incompatible behaviour within silicate minerals, relative to silicate melts and aqueous fluids [1–5]. Their preference for entering silicate melts and aqueous fluids implies that their distribution within the mantle and crust is controlled by fluid transfer processes between reservoirs, such as magmatic melting, degassing and dehydration reactions [6–8]. Halogens are, therefore, useful tracers of volatile transport processes operating both within the mantle and between the mantle and crust. The low ppm to ppb concentrations of Cl, Br and I within mineral assemblages have previously led to analytical challenges and held back the understanding of halogen behaviour within the mantle. However, recent advances with neutron-irradiated noble gas mass spectrometry (NI-NGMS) [9,10] are advancing our understanding of halogen and volatile behaviour within the mantle and at crust–mantle interfaces [11–18]. The

volatile content of the mantle is important to understand and quantify, as it affects properties such as the melting point of mantle rocks and minerals, their viscosity and their rheology [19]. Over geological time, the composition of the mantle is influenced through the loss of volatiles to the surface through volcanism and their return via subduction. Whether these processes are in balance or not can, therefore, affect mantle rheology, modes of convection, convection vigour, and thus heat transfer, and the rate of planetary cooling, ultimately influencing the style of plate tectonics at the surface of Earth [20]. Halogens can also be mobilised from the mantle during large-scale magmatic processes such as large igneous province (LIP) eruptions, potentially contributing to extensive ozone depletion and the decline of the biosphere [21]. Better insight into and understanding of halogen behaviour within the mantle may, therefore, help us to understand how the geosphere evolves over time and interacts with the atmosphere, hydrosphere and biosphere.

During the process of subduction, halogens are expected to become progressively depleted from the crust as subduction progresses, as they partition into silicate melts and aqueous fluids generated during the breakdown of hydrous mineral phases such as amphibole, antigorite, apatite, mica and talc. The increased compatibility of F in hydrous minerals leads to fractionation of F from the heavier halogens and its retention to the deeper mantle [22]. In contrast, Cl, Br and I are not expected to be fractionated but, instead, are thought to be almost entirely stripped from the subducting slab by the released fluids, after which they are then transported into and act as agents of metasomatism in the overlying mantle wedge. The halogen content of the mafic and ultramafic material of the mantle wedge may, therefore, provide insight into the halogen systematics of fluids released during subduction. Fluid inclusions trapped within these rocks provide information on the composition of fluids involved in high-pressure (HP) or ultra-high-pressure (UHP) eclogite-facies metamorphism and the halogen systematics of the deeper mantle [11], and allow us to study the effects of high P-T fluid–mineral interactions on the compositions of both high-pressure mineral phases and supercritical fluids. Despite being a greater source of both $H_2O$ and volatiles, little focus has been placed on the potential for the subduction of continental crust to induce mantle metasomatism and thus volatile transport between the crust and mantle.

This study uses electron-probe micro-analysis (EPMA), time-of-flight secondary ion mass spectrometry (TOF-SIMS) and NI-NGMS to constrain the halogen composition of UHP mineral and fluid inclusions from the Western Gneiss Region, Norway. The fluid composition is used to assess the halogen systematics of deeply subducted continental crust, close to the interface between crust and mantle, during high P-T metamorphism.

## 2. Geological Setting

The Caledonides of Scandinavia and Greenland represent the northern segment of the Caledonian-Appalachian-Tornqvist orogenic belt that formed during the Palaeozoic [23]. This segment was split along its axis by the opening of the Atlantic ocean. The Scandinavian part of the orogen comprises a pile of far-travelled thrust nappes derived from the continental margins of the Baltica and Laurentia palaeo-continents, sandwiched between which are arc and marginal basin terranes derived from within the Iapetus palaeo-ocean basin [23]. Orogenesis followed the closure of Iapetus, which culminated in the Scandian continental collision of Baltica and Laurentia [24–26], commencing at ca. 430 Ma and continuing into the Mid-Devonian (ca. 380 Ma) [27]. Transient subduction of the Baltica continental margin to depths of more than 100 km beneath Laurentia resulted in HP and UHP metamorphism of the Baltican Fennoscandian basement and its cover [28,29], manifested as widespread occurrences of eclogites within gneisses now exposed in a series of basement windows that emerge through the nappe pile in the orogenic hinterland [30]. The oceanic allochthons are not known to have undergone eclogite-facies metamorphism. The Caledonide nappe pile was translated along a decollement horizon of Tremadoc black shales (Alum Shale Formation) that represents a marine transgression that flooded much of what is now Scandinavia [31] just prior to the Caledonian orogeny.

The Western Gneiss Region (WGR) in southwest Norway is the largest of these basement windows, occupying an area of the approximately 50,000 km² [32,33] between Trondheim and Bergen (Figure 1). It is a world class example of a well-preserved and well-exposed, giant continental crustal eclogite terrain. It is chiefly made up of Proterozoic orthogneisses of the Fennoscandian shield and their Neoproterozoic to Ordovician metasedimentary cover. The overlying allochthons locally occupy linear inliers within the WGR, where they have been infolded and/or imbricated into the basement [34]. Those derived from Baltica basement or cover have undergone Scandian eclogite-facies metamorphism and possibly earlier, Ordovician high-pressure metamorphism [35] though the infolded oceanic allochthons only show greenschist to amphibolite metamorphism [36]. In the main nappe pile outside the basement windows, HP and UHP eclogite-facies metamorphism was widespread within allochthons derived from Baltica [35,37] including the Lindås Nappe near Bergen, in which mid-to-late Proterozoic granulite-facies anorthosite underwent early Scandian eclogite-facies transformation related to fluid ingress [37].
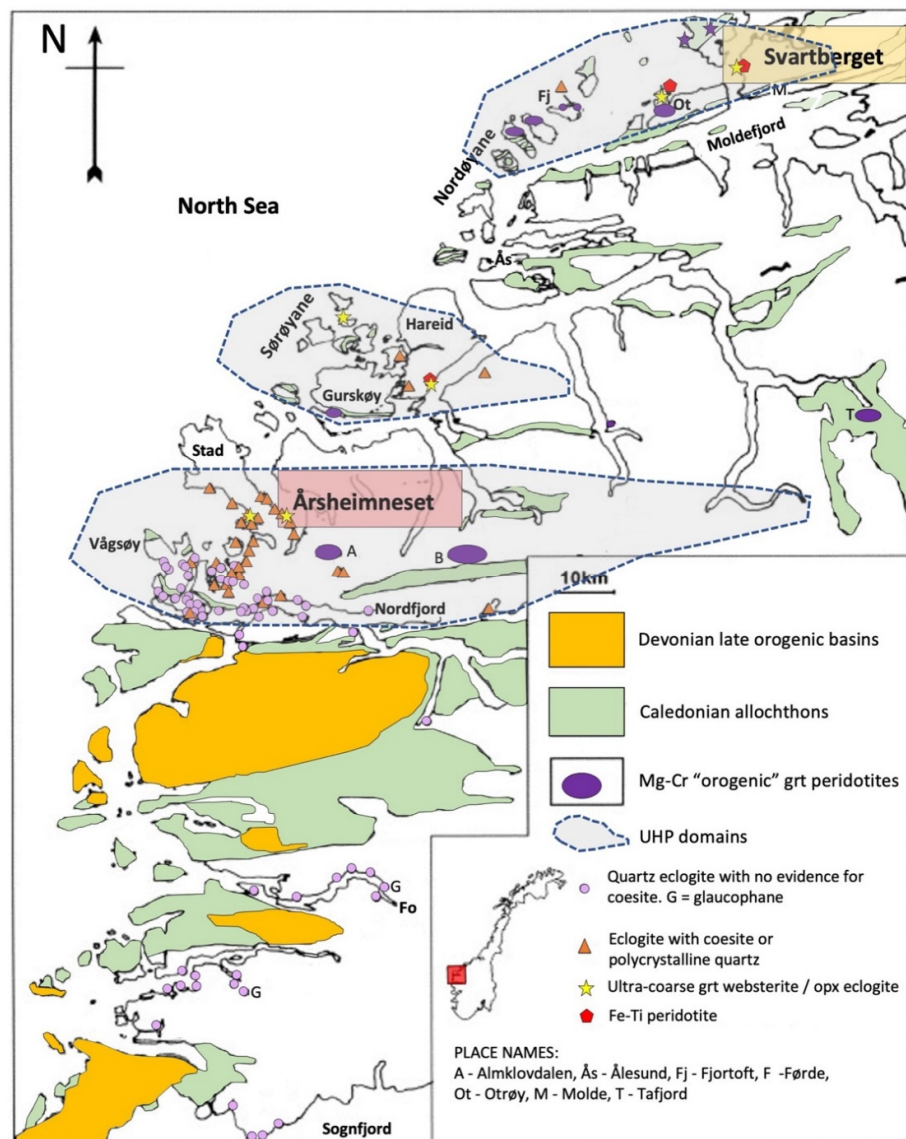


**Figure 1.** Map of the WGR, western Norway, redrawn after [33], showing the petrographic context and location of the two areas of Årsheimneset and Svartberget in this study. UHP domains modified from [38].

The Scandian metamorphic overprint in the WGR shows gradational change from the south east, where eclogites are absent, towards the north west, where eclogites become ubiquitous [33] within both basement rocks and cover sequences [33]. Peak conditions of Scandian UHP metamorphism are estimated at 800 °C and up to 3.6 GPa [36], occurring at ~418 Ma, based on averages from U-Pb and Nd-Sm isotopic dating [39–41]. Ultra-high-pressure eclogites and felsic rocks, as indicated by the presence (or former presence) of coesite or by thermobarometric P-T determinations, occupy three distinct domains in the coastal region of the northern half of the WGR, northwards from Nordfjord (Figure 1). This overall pattern of increasing P&T towards the NW results from the subduction of the WGR rocks below the Laurentian margin and, where UHP conditions are recorded, below the Laurentian sub-continental lithospheric mantle [33]. In detail, this pattern has been disrupted by large-scale imbrication of the WGR basement and cover, as shown by major thrust-related shear zones [42,43]. Importantly, these shear zones, marked by belts of disrupted allochthons, display swarms of Mg and Cr-enriched orogenic (mantle-derived) ultramafic bodies, some of which are garnet bearing. They coincide with domains of UHP eclogites within the gneisses. These ultramafites are thought to derive from the Laurentian SCLM, having been entrained from above the subducting WGR slab [44]. These shear zones are, therefore, taken to represent the uppermost part of the subducting Baltica continental slab that lay close to the interface with the overlying mantle wedge [33,36]. The shear zones were partly remobilised as a large normal-sense shear, the Nordfjord-Sogn Detachment, which accommodated exhumation of the WGR and has been termed the "mantle-exhumation surface" [36]. Proximity of a mantle wedge that, presumably, overlays the subducting Iapetus Ocean crust prior to collision may be significant for the fluid evolution of the WGR HP and UHP rocks.

Eclogite facies rocks within the WGR have formed via the metamorphism of a variety of protoliths including gabbro; mafic, anorthositic and felsic granulites; pelites, and layered mafic-ultramafic intrusions [45–49]. The widespread presence of phengite in granitoid orthogneisses in the WGR [36] and local occurrences of omphacite-bearing felsic gneiss [50] suggest that transformation of the predominant gneissic basement has undergone extensive high-pressure metamorphism, although common preservation of magmatic or charnockitic mineral assemblages suggests that the transformation process was inefficient [50]. The prominent metabasic eclogites show evidence for formation by transformation of gabbro or granulite [47,49–52] by a combination of deformation and hydration. Zoning and inclusion suites in garnets show that eclogites formed from amphibolite [46,53] that can, itself, sometimes be shown to have formed on a continuous Scandian prograde subduction P-T path that led to eclogite formation from a gabbroic or granulitic protolith [54,55]. Similarly, felsic 2-pyroxene granulites have been transformed to eclogite-facies mineral assemblages by hydration [37,50].

Previous studies of fluid inclusions in mafic eclogites in the WGR and the overlying Lindås Nappe suggest that the eclogite facies fluid phases were $N_2$–$CO_2$–$H_2O$ and $H_2O$–NaCl brines [56–60] and that there is no systematic pattern for the regional distribution of fluid composition in the WGR [33].

While the Mg-Cr-enriched orogenic ultramafic rocks mentioned above are undoubtedly derived from the mantle, another important group of Fe and Ti-enriched, eclogite-facies ultramafic rocks and associated mafic eclogites are considered to have formed from Proterozoic mafic-ultramafic intrusions that were autochthonous with respect to the Fennoscandian basement rocks of the WGR prior to Caledonian orogenesis [61,62]. In the northern WGR, near Molde, these commonly host metasomatic vein-selvage systems formed under diamond-facies UHP conditions [63,64]. They are considered to have formed by injection of a granitoid melt or silicate-rich aqueous fluid along fractures and that percolated into the peridotite wall rock [63,64]. The selvages are dominated by ultra-coarse-grained, decussate-textured garnet-phlogopite websterite or orthopyroxene eclogite. Very similar websterites are also found as pods in the gneiss in the same area [63,65] and probably had the same metasomatic origin. Further south along the coast at Søroyane

and in the Selje area (Figure 1), identical websterites are interlayered with coesite eclogite; these include the classic "pegmatitic" enstatite eclogites in the Selje area near Nordfjord [66], where ultra-high-pressure metamorphism was first recognised in the WGR [30,67,68]. Similarities in texture, composition and the presence of UHP vein systems [69] suggest, again, a metasomatic origin for these websterites/eclogites due to an influx of a silicate- and large-ion-lithophile-rich fluid or granitoid melt. This lithology, along with its associated gneiss and metabasic eclogite are the subject of this study. It is noteworthy that there is evidence of Scandian partial melting in the gneisses and eclogites in the northern half of the WGR, where these lithologies are found [70–72].

The pre-Scandian relationships of eclogites with their host gneisses in the WGR are nearly always obscured by shearing and amphibolite-facies retrogression. Eclogites and their adjacent hosts sometimes show a common HP or UHP evolution. A small number of protolith ages are Meso- to Neoproterozoic, suggesting emplacement into the Baltica crust long prior to Scandian orogenesis [45,73,74]. Rarely, primary intrusive relationships have been preserved [49]. This limited evidence suggests that most metabasic eclogites were magmatic intrusions into the Baltica crust prior to the Caledonian orogenic cycle. There are no available protolith ages for the Fe-Ti ultramafites and associated eclogites, but geochemical similarities with eclogites having Proterozoic protolith ages, and with other Proterozoic cratonic magmatic suites [75], suggest that these, too, were autochthonous to the Baltic craton. There is, to date, no evidence that eclogites and ultramafites in the WGR had origins in the Iapetus oceanic realm.

### 3. Sample Locations and Petrography

Two locations were selected for this study—Svartberget, near Molde in the northern UHP domain and Årsheimneset, near Maløy, in the southern UHP domain (Figure 1). The Svartberget ultramafic body outcrops in the area where the highest metamorphic pressures recorded in the WGR have been determined from the presence of microdiamond [76] and thermobarometry [65]. The Årsheimneset eclogite-websterite body, referred to as "Sandviknaes" in early studies [67,68], is one of a cluster of massifs in the area near Selje, in which the first discoveries of coesite were made [30,77].

The Svartberget ultramafic body [63,64] has a lens outcrop form with dimensions of approximately 60 × 40m. It is enclosed within migmatitic biotite + plagioclase + K-feldspar + quartz orthogneiss with minor garnet and sillimanite. The dominant lithology in the body is spinel-garnet-peridotite. This is cut into >700 angular blocks by a dense array of fracture-fill veins cored by garnetite, eclogite, omphacite clinopyroxenite, granitoid phengite- or cpx-bearing pegmatite. Approaching these veins, the initial change in the host olivine websterite is the appearance of Ti-clinohumite and minor magnesite rimmed by dolomite. Then, opx increases, phlogopite appears and olivine disappears. Adjacent to the vein core, all phases become extremely coarse grained and have a randomly orientated, decussate texture. Locally, at vein intersections and near the margin of the body against gneiss, phlogophite dominates to give a decussate-textured glimmerite. Multiphase micro-inclusions in garnet and pyroxene from vein-fills contain similar silicate phases to those in the matrix along with feldspars, carbonates, sulphates, sulphides, phosphates, rutile, allanite, unidentified Al–Fe–Mg silicates and microdiamond. The migmatitic character of the host gneiss suggests that the metasomatic additive melt or fluid phase was broadly granitoid in composition and sourced locally, probably represented by prominent leucosomes in the gneiss. This is supported by the composition of felsic vein cores within the body and by mass balance calculations [64]. Further support for a local source is the highly radiogenic Sr isotope composition of cpx in the pyroxenite selvages and mid-Proterozoic to Neoproterozoic U-Pb ages for inherited zircon cores in the garnetite (the zircon appears to have been introduced as solid grains, advected by a viscous fluid [63,78].

P-T estimates on the ol-grt-websterite host by [76] were 800 °C, 34 kb but they obtained a significantly higher pressure of 55 kb for the websterite veins, which was taken to indicate that vein formation occurred after an increase in P following equilibration of

the host. However, similar conditions for both host and selvage but at slightly lower T (764 ± 7 °C, 33.6 ± 2.2 kb for the ol-grt-websterite and 792 ± 9 °C, 38.5 ± 2.7 kb for the vein selvage) were calculated by [63]; these are, nevertheless, consistent with the presence of diamond.

The most robust ages for the UHP metamorphism and metasomatism at Svartberget are given by concordant U-Pb dates from overgrowths on zircon in a garnetite vein core at 410.6 ± 2.6 Ma and 411 Ma 403.0 ± 5.6 Ma for a websterite selvage [63], consistent with many ages for HP and UHP rocks in the WGR. The host migmatitic gneiss yielded a younger age, ca. 401 Ma, suggesting that the zircon growth in the host rocks continued after vein formation.

The Årsheimneset body is a large, tabular mass with plan size approximately 50 × 40 m. It is internally layered and folded, mainly comprising coarse-grained orthopyroxene eclogite or garnet websterite and garnet orthopyroxenite with finer-grained quartz eclogite and retrogressive amphibolite [63,67,69]. No olivine-bearing varieties have been found. Samples come from a small roadside cutting that exposes a complete section through the body approximately 3 m thick and dipping steeply to the east. A core of coarse-grained quartz eclogite ~2 m thick is sandwiched between layers of coarse-grained and locally very coarse-grained phl-carbonate grt websterite grading to opx eclogite. The lower grt websterite layer encloses discrete pods of quartz eclogite similar to the central layer. Near the margin, eclogite and websterite are replaced by foliated retrograde amphibolite, as is commonly observed in eclogites in the WGR.

A previous description of the quartz eclogite [69] showed garnet to be compositionally zoned with an outward increase in Mg number and decrease in Mn and Ca. Cores enclose inclusions of omphacite and pargasitic amphibole, while higher Mg rims have only omphacite. Evidently, these garnets grew by consuming an amphibole-rich eclogite precursor. Garnets in grt websterite were shown to be xenoblastic and poikiloblastic, lacking compositional zoning except for a narrow retrograde rim adjacent to matrix Ca-amphibole. Abundant inclusions of diopsidic cpx are enclosed in spongey cores, but garnet rims have fewer cpx inclusions and, instead, include coarser phlogopite, orthopyroxene, polycrystalline quartz (after coesite) and zircon. The appearance of phl and qz inclusions only in the rims is consistent with an influx of a K and silica-rich fluid or melt after initial garnet growth in a cpx-rich precursor. Patchy concentrations of coarse-grained magnesite in the grt-websterite are consistent with UHP conditions [ 60,68]; nevertheless, $X_{CO_2}$ in the fluid was probably low [68]. O and C isotope analyses of carbonates [79] gave $\delta^{13}C = -4.5‰$ and $\delta^{18}O = +9.7 ‰$. Peak P-T conditions for the grt websterite were estimated at 696 ± 6 °C, 35.3 ± 0.3 kb [63] and 715 ± 7 °C, 29.5 ± 0.7 kb.

Both the eclogite and grt websterite layers enclose mica-rich lenses and seams with a narrow rim of garnet and quartz [63,69]; inclusions of palisade polycrystalline quartz indicate prior presence of coesite. A phengite + quartz-cored vein in the quartz eclogite has an outer halo of omphacitite passing abruptly into the host eclogite. Similar garnet-free "bleach zones" have been attributed to fluid action in eclogites (see, e.g., [80] for an example in New Caledonia). The micaceous seams have a composition similar to magmatic alkali-feldspar granite and, like the vein cores at Svartberget, are rich in apatite and zircon [63]. $^{87/86}Sr$ in cpx from the grt websterite is highly radiogenic, but unsupported by high Rb/Sr, suggesting a pervasive influx of radiogenic Sr from an external source [81].

Xenocrystic zircon cores in mica-cored veins gave discordant U-Pb isotope compositions with upper concordia intercepts at c. 1500 Ma or older, consistent with introduction of zircon xenocrysts derived from the host gneiss and entrained in a melt/fluid. Rims or unzoned zircons clustered on the concordia to give robust ages for metasomatism under UHP conditions at 414.0 ± 5.6 Ma, identical within error to metamorphic zircon from the quartz-eclogite at 411.4 ± 5.3 Ma [63].

The country-rock in the surrounding area (Stadlandet) is predominantly a granodioritic, migmatitic orthogneiss [48]. Bulk-fraction U-Pb zircon ages indicate mid-Proterozoic protoliths and "reconstitution"or new zircon growth at c. 400 Ma [82]. Adjacent to the

lower margin of the eclogite, a platy 2-mica, 2-feldspar gneiss is probably a highly strained equivalent to this and it yielded a concordant U-Pb age for zircon rims of 417.0 ± 10 Ma [63].

Samples collected for this study from Årsheimneset and Svartberget (Figure 1) consist of both anhydrous and hydrous minerals (Table 1) derived from eclogite facies mafic-ultramafic bodies hosted within the gneiss country rock. The following descriptions are based on optical (Figure 2) and Raman spectroscopy of samples. Mineral fractions separated from samples for NI-NGMS analysis are listed in Table 1 and sample preparation details are presented in Section 4.1.

**Table 1.** Summary of sample collection location, protolith lithology, major and minor mineralogy and prepared mineral fraction(s) separated from WGR samples. (alb = albite; amp = amphibole; bt = biotite; cc = calcite; chu = clinohumite; cpx = clinopyroxene; gt = garnet; mon = monazite; ol = olivine; opx = orthopyroxene ; opq = opaques; phe = phengite; qtz = quartz; rt = rutile; spl = spinel; ; zr = zircon).

| Sample ID | Location in Figure 1 | Lithology | Major Phases | Minor Phases | Prepared Fraction |
|---|---|---|---|---|---|
| QC26C | Årsheimneset | Gneiss | Alb-qtz-gt | Ph-ap-zr | Ph, gt |
| QC26E | Årsheimneset | Eclogite | Gt-cpx-qtz | Rt-ap-zr | Gt, qtz |
| QC26G | Årsheimneset | Garnet websterite | Gt-bt-cpx-opx-cc | Amp-rt-opq-spl-zr | Gt, bt |
| QC26H | Årsheimneset | Garnet websterite | Gt-bt-cpx-opx | Qtz-amp-rt-ap-mon | Gt, qtz, bt |
| QC36A | Svartberget | Olivine websterite | Gt-cpx-opx-ol | Amp-opq-spl | Ol, gt |
| QC36C | Svartberget | Garnet peridotite | Gt-ol-opx-cpx | Chu-opq | - |
| QC36D | Svartberget | Garnet websterite | Gt-bt-opx-cpx | Amp-rut-zr-opq | Gt, bt |
| QC36G | Svartberget | Garnet websterite | Gt-bt-cpx-opx | Amp-rt-zr-mon | Gt, bt |
| QC36Q | Svartberget | Leucogneiss | Qtz-afs-bt-ph | spl | Qtz |
| QC36U | Svartberget | Garnetite | Gt-bt-cpx-opx-ap | Amp-ph | - |

*3.1. Årsheimneset Samples*

QC26C is a garnet muscovite gneiss and represents the host rock to the Årsheimneset eclogite-websterite body. This is a common lithotype in the Stadlandet-Norfjord area. The matrix is Ab and Qz with subordinate Grt, Kfs (microcline), Mu and accessory Zrn and Ap. Grt forms xenoblastic to subidioblastic, medium- to coarse-grained porphyroblasts with abundant inclusions of Qz and Fsp (Figure 2a). Mu forms isolated grains dispersed throughout the quartzo-felspathic matrix. Accessory Ap occurs in the matrix and as inclusions within Grt.

QC26E is a quartz eclogite that forms a lens 1 m in length isolated within the lower websterite layer [63,69]. It is coarse grained, granoblastic and dominated by Grt, Omp and Qz with minor Rt and accessory Ap, Zrn and sulphides (Figure 2b). Poikiloblastic secondary Ca-amphibole encloses and replaces Omp and Grt. Omp hosts inclusions of Rt and Ap and displays abundant, small (up to 10 μm) exsolved Qz needles, each associated with a small patch of secondary Amp. Ab-Di symplectite lies along Omp grain boundaries. Grt is subidioblastic or idioblastic and hosts numerous inclusions of Rt, Ap, Ca-Amp or multi-phase inclusions (MPIs), the amphibole lying preferentially in the Grt cores. Qz is in the matrix but also forms inclusions in Grt and Omp. Accessory Ilm, Py and Ccp occur both throughout the matrix and as inclusions in the other phases.
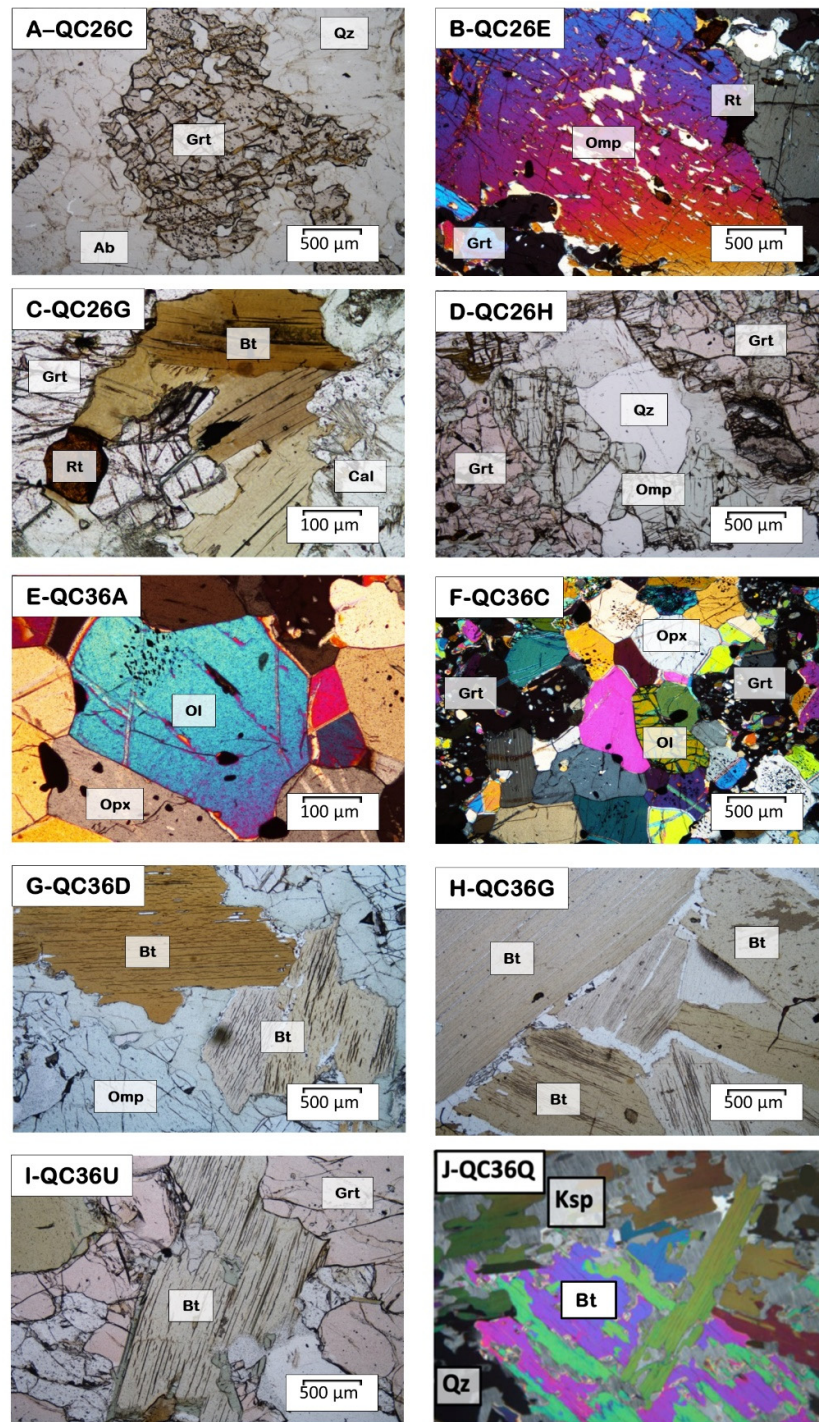
**Figure 2.** Photomicrographs showing key features of samples. (**A–D**)—Årsheimneset; (**E–J**)—Svartberget. (**A**) QC26C gneiss—PPL; (**B**) QC26E eclogite—XPL; (**C**) QC26G garnet-phlogopite websterite—PPL; (**D**) QC26H garnet websterite—PPL; (**E**) QC36A garnet websterite (vein selvage)—XPL; (**F**) QC36C garnet lherzolite (outermost vein selvage)—XPL; (**G**) QC36D garnet-phlogopite websterite (vein selvage)—PPL; (**H**) QC36G phlogopite-rich part of opx eclogite vein selvage—PPL; (**I**) QC36U garnetite (vein core)—PPL; (**J**) Pegmatite lens showing Bt + Ksp intergrowth after phengite—XPL. Ab = albite, Bt = biotite or phlogopite, Cal = calcite, Grt = garnet, Ksp—alkali feldspar (perthite) Ol = olivine, Omp = omphacite, Opx = orthopyroxene, Qz = quartz and Rt = rutile.

QC26G is a carbonate-bearing opx eclogite from the upper websterite layer approximately 20 cm from some small garnet-mica-quartz veins [63,69]. The rock is medium to coarse grained, decussate and comprised of Grt, Omp, Opx and Phl (Figure 2c) with minor Ca-Amp, Cc and Fe-Ti oxides and accessory Rt, Spl and Zrn. Omp has inclusions of Phl, Ca-Amp and Tur. Tiny inclusions of Qz and fluid inclusions appear as planar trails through these grains, and they have narrow symplectite rims. Grt forms xenoblastic grains with a only few inclusions of Phl, Ca-Amp and Tur. Grt is also included in the other matrix phases. Phl is coarse grained in the matrix and forms smaller inclusions within Grt and Omp; with larger grains having been altered to Chl at grain margins.

QC26H is a medium- to coarse-grained Opx eclogite (Figure 2d) from the inner edge of the upper websterite and is composed of Grt, Opx, Omp and Phl, with minor Ca-Amp and Qz and accessory Ap, Rt, Zrn, Fe-Ti oxides, Py, Ccp and Mnz. The sample also contains a Bt + Qz cored, Grt-rimmed vein. The opx-eclogite shows a weak preferred orientation of elongate Opx and Ca-Amp grains. Pale green Ca-Amp is apparently in textural equilibrium with the pyroxenes and Grt. Matrix Qz shows a polycrystalline texture possibly indicative of prior coesite. Phl is abundant throughout the matrix but also occurs as inclusions in Omp and Grt. Opx grains are elongate with planar trails of fluid and quartz inclusions. Grt porphyroblasts are inclusion rich, containing Jd, Omp, Bt, Qz, blue-green Amp, Ap and MPIs. Apatite also occurs in the matrix. Opaque phases include pyrite and chalcopyrite.

### 3.2. Svartberget Samples

QC36A is a medium-grained, granoblastic olivine garnet websterite from the outer part of a vein selvage equivalent to metasomatic zone 1c of [64]. Essential phases are Grt, Ol, Opx and Cpx with minor Ca-Amp, Mt and Spl. Ol is anhedral to subhedral (Figure 2e) with trails of Fe-Ti oxide. Cpx shows rods of exsolved Cr-Spl. Opx encloses exsolved opaque oxide and fine Cpx lamellae. Grt is xenoblastic and rimmed by 2-Px-Spl-Amp kelyphite associated with coarser Ca-Amp.

QC36C is a fine- to medium-grained, granoblastic garnet peridotite from the outermost part of a metasomatic selvage, equivalent to Zone 1b of [64]. It consists of Grt, Ol, Opx and Cpx with minor Chu and accessory Cr-Spl and Fe-Ti oxides. Cpx has exsolved Fe-oxide or Cr-Spl while Opx displays fine Cpx exsolution lamellae. Grt forms masses of xenoblastic grains hosting abundant inclusions (Figure 2f) of Px and Ol. Kelyphite reaction rims around garnets in contact with Ol are much less pronounced than in QC36A. Chu is anhedral, with an irregular distribution. It is locally replaced by symplectic intergrowths of Ol and Ilm.

QC36D is a coarse-grained, decussate garnet websterite from a vein selvage equivalent to zones 2 or 3 of [64]. It comprises essential Grt, Opx, Cpx and Phl, minor Ca-Amp and accessory Rt, Mt, Zrn and Ccp (Figure 2g). Grt is fine grained, subidioblastic to xenoblastic and either inclusion poor or occasionally inclusion rich. Cpx grains are lath shaped with inclusions of Phl and earlier Ca-Amp. Opx is elongate and rich in inclusions of Phl and has exsolution lamellae of Cpx. Opx and Cpx are frequently intimately intergrown. Phl is distributed throughout the sample as a matrix phase and also occurs as inclusions in all other phases. Late, pale green Ca-Amp is poikiloblastic, overgrowing all other matrix phases. Rt is ubiquitous in the matrix and is included in Grt and Px's.

QC36G is a very coarse-grained, decussate, phlogopite enstatite eclogite that lay immediately adjacent to a zoned garnetite-clinopyroxenite vein core, equivalent to metaomatic transition zones 4 or 5 of [64]. It comprises essential Grt, Opx, Cpx, Phl and Qz with minor Ca-Amp in apparent textural equilibrium with Px and Grt, plus accessory Rt, Zrn, Mnz, Ccu and Py. Grt is subidioblastic and inclusion poor. Cpx is omphacitic, hosts inclusions of biotite, has exsolved needles of Qz and is rimmed by Di-Ab symplectites. Opx also has inclusions of Phl and is commonly fractured. Phl is ubiquitous throughout the sample. Abundant Qz is present in interstices between Phl grains.

QC36U is a garnetite from a zoned vein core equivalent to metasomatic vein Zone 6 of [64]. It predominantly consists of coarse Grt, with minor Phl, Opx, Ca-Amp and Ap and accessory Ph, Spl, Zrn, Mnz and opaques. Interstices between Grts are filled by small grains of Ap, Ca-Amp, micas and MPIs. Inclusions in Grt include Ca-Amp, Chl, Spl and Fe-oxide. Opx shows partial replacement by pale greenish biotite. Apatite is often found in association with monazite.

QC36Q is a granitoid pegmatite that forms an elongate lens within the ultramafite body close to its margin. It forms the core to a metasomatic selvage of glimmerite and phlogopite clinopyroxenite [63] and appears to connect with the host migmatitic gneiss. It probably represents the metasomatic agent, emanating from the host gneiss, that has generated the garnetite-websterite vein system in the peridotite. The rock comprises abundant qz, afs, bt and mu. Patches of: (i) coarse-grained, bluish qz alternates with (ii) intergrowths of bt and mu within poikiloblastic microperthite. The two micas have a systematic crystallographic orientation within the feldspar and the intergrowths are probably pseudomorphs after large phengites.

### 3.3. Multi-Phase Solid Inclusions (MPIs)

MPIs are inclusions within a host mineral that contain multiple solid mineral phases, sometimes along with fluid phases and/or cavities. They are thought to form via the crystallisation of daughter crystals from fluid phases that were trapped within the host mineral during its growth. Therefore, they may provide information on the compositions of the fluid present at the conditions of entrapment, provided that the timing of entrapment can be established [60]. When considering inclusions, it is, therefore, crucial to establish the relative timing of inclusion formation and entrapment. Omphacite- and garnet-hosted MPIs of various sizes—from tens to hundreds of microns in diameter—are abundant within samples from both Årsheimneset and Svartberget. These MPIs are similar in appearance to multi-phase inclusions in a wide range of other HP-UHP rocks [83]. Many of the inclusions also contain trapped fluid phases along with the solid phases (Figure 3). This study focuses primarily on the MPIs within garnet but also investigates inclusions within quartz and olivine.

### 3.3.1. Garnet-Hosted Inclusions

MPIs are inclusions within a host mineral that contain multiple solid mineral phases, sometimes along with fluid phases and/or cavities. They are thought to form via the crystallisation of daughter crystals from fluid phases that were trapped within the host mineral during its growth. Therefore, they may provide information on the compositions of the fluid present at the conditions of entrapment, provided that the timing of entrapment can be established [60]. When considering inclusions, it is, therefore, crucial to establish the relative timing of inclusion formation and entrapment. MPIs are found within garnets from all lithologies analysed in this study. The majority of MPIs exist as densely packed clusters within the cores of host crystals, or as planar trails that taper off and terminate within the host crystal. Inclusions close to the grain boundaries of the garnets are rare. Groups of MPIs are often elongate, with similar ranges in size and follow the same orientation through the crystal (Figure 3). Based on these observations, we interpret the MPIs as being primary inclusions that became trapped at eclogite facies conditions.

Figure 4 shows a collage of BSE images of representative MPIs inset within an Mn/Fe-distribution map of the host garnet. The MPIs have various shapes and sizes. Some have flat faces and sharp contacts with the host mineral, whilst some are irregular and poorly formed. The shapes of MPIs range from equant polygons to irregular and elongate with offshoot structures. MPIs range in size from small scale (~5 µm) to large scale (~500 µm). Generally, the number of daughter crystals and solid phases present within MPIs is less than four. The following phases were identified within MPIs but are by no means an exhaustive list: amphibole, apatite, biotite, calcite, chlorite, clinopyroxene, NaCl (halite),

ilmenite, KCl (sylvite), K-feldspar, monazite, opaques (e.g., FeO, FeS, FeCuS, PbS) plagioclase feldspar, quartz, rutile, phengite and zircon. Often, MPIs contain unidentified phases with Al-Mg-Si ± Ca ± Fe chemistry, which may or may not be hydrous in nature, e.g., various types of amphibole and talc. No carbon-bearing phases, indicative of diamonds, as found in the WGR in previous studies [76,78], were observed in this study. This assemblage of solid inclusions is similar to that found in previous studies with the exception of carbon-bearing phases including diamond [76,78] that were not observed in our samples; the presence of native C and sulphides was taken to indicate a relatively reducing composition [76] (a recent study [84] using garnet oxybarometry in a vein core yielded $fO_2$ ranging from −1.7 to −2.1 ΔlogFMQ units).
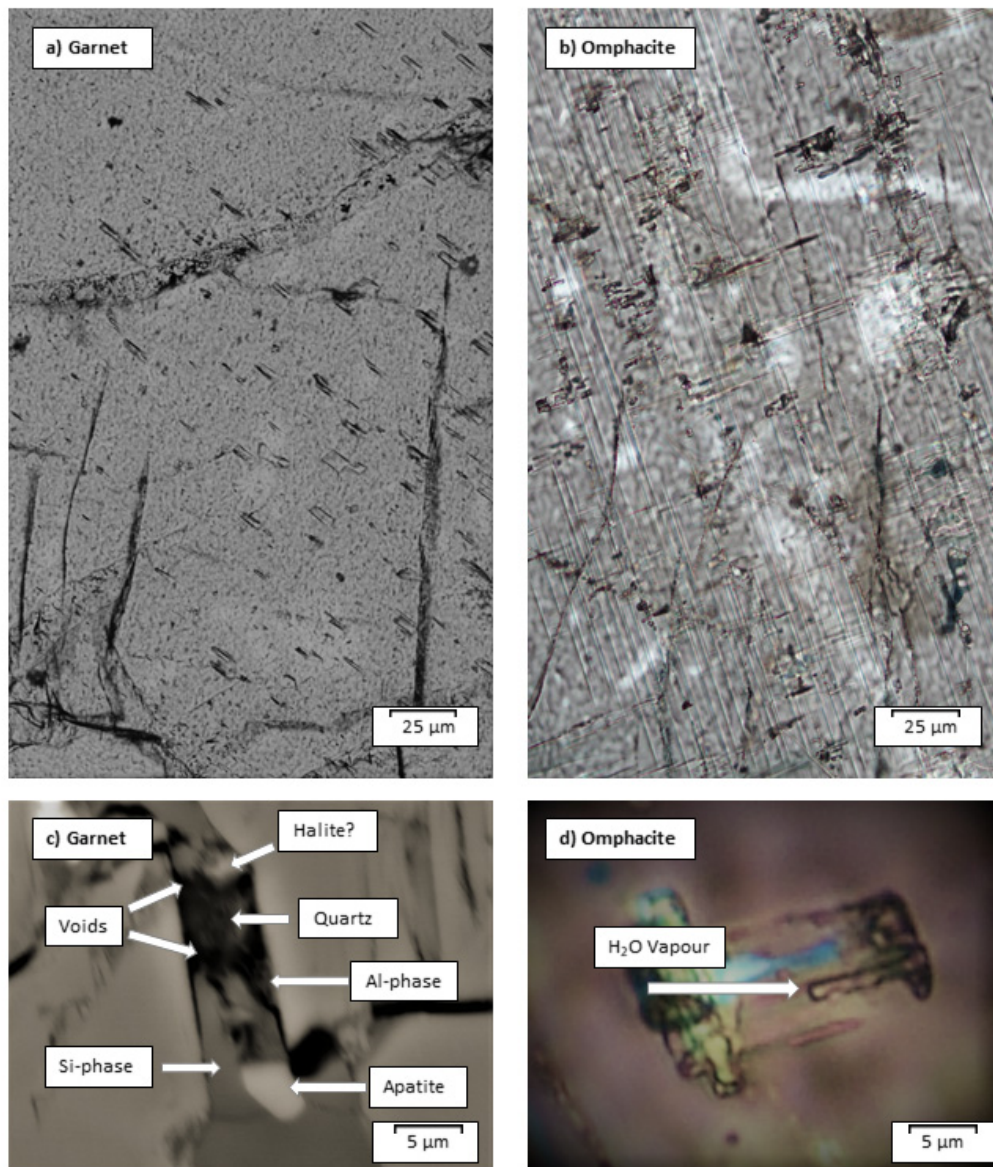


**Figure 3.** Photomicrographs of (**a**) garnet- and (**b**) omphacite-hosted inclusions, sample QC26E quartz eclogite, Årsheimneset. (**c**) Back-scattered electron image of a multi-phase inclusion in garnet in sample Q26G, opx eclogite, Årsheimneset, showing voids and solid phases (apatite, quartz, halite? and Al and Si phases). (**d**) Photomicrograph of omphacite-hosted fluid inclusion showing trapped $H_2O$ vapour in sample QC26E.
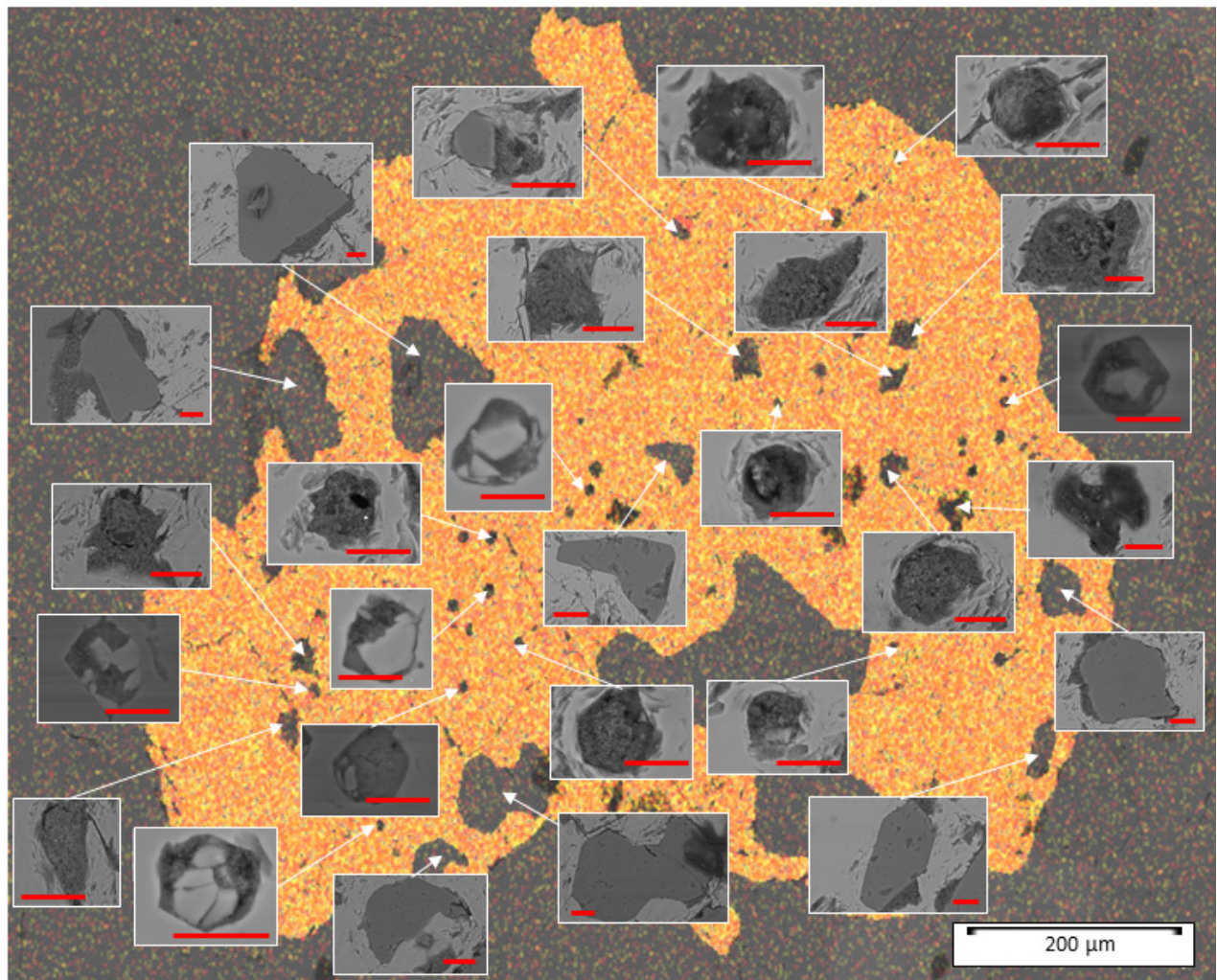
**Figure 4.** Collage of back-scattered electron images of MPIs superimposed on an Mn/Fe-distribution map of the host garnet, showing the typical abundance and distribution of MPIs in host minerals of this study. MPIs comprise both voids and various solid phases (quartz, micas, apatite, feldspar and unidentified phases with Al-Mg-Si ± Ca ± Fe chemistry). The size of MPIs varies from tens to hundreds of microns. Inset scale bar = 15 microns. Sample QC26C, gneiss, Årsheimneset.

In addition to containing solid phases, MPIs also host small-scale fluid phases (Figure 3d), along with numerous voids, which likely represent previously opened fluid inclusions. Numerous fluid inclusions are present in garnet—and also in pyroxene, olivine and quartz—as both elongate inclusions forming planar trails and as spherical-ovoid clusters within the cores of host crystals (Figure 3a,b). Like MPIs, the fluid inclusions are found in the cores of host crystals and are rarely seen at grain boundaries. Garnet-hosted fluid inclusions are typically <10 µm in diameter, with some larger inclusions also containing a vapour bubble. Fluid inclusions are notably more abundant in samples from Årsheimneset than in samples from Svartberget.

### 3.3.2. Omphacite-Hosted Inclusions

Many of the characteristic MPIs and fluid inclusions described in garnet samples are also present in samples of omphacite. Previously, it was shown that the halogen ratios of omphacite-hosted fluid inclusions in samples from the WGR have a similar range in Br/Cl and I/Cl ratios to those of garnet-hosted inclusions [60]. The petrography and nature of fluid inclusions in this study precludes the isolated trapping of two different fluids by

garnet and omphacite at different times, and instead suggests a single fluid interacted with host minerals. Given the petrography and nature of MPIs in this study, plus their similarities with those in a previous study of WGR samples [60], garnet-hosted fluid inclusions can be assumed to provide sufficient insight into the halogen systematics of fluids at depth within the WGR.

## 4. Analytical Methods

Aliquots of separated mineral fractions (Table 1) were neutron irradiated to convert Cl, Br and I into noble gas isotopes of Ar, Kr and Xe, respectively [9,10], which were then measured in NI-NGMS analysis. Noble gases were liberated from mineral grains using in vacuo crushing and fusion by $CO_2$ laser. Additionally, F, Cl, Br and I were also investigated by in situ analytical and spatial mapping using electron-probe micro analysis (EPMA) and time-of-flight secondary ion mass spectrometry (TOF-SIMS).

### 4.1. Sample Selection and Irradiation

Rock samples were crushed then sieved, and mineral grains identified and hand-picked under a binocular microscope. Mineral separates were then washed in acetone and rinsed with de-ionised water. Following rinsing, aliquots of the samples were then packed in Al-foil and sent for irradiation. The samples were irradiated on the 24 July 2012, for 24 h, at the high flux reactor RODEO facility, Petten, Netherlands, with constant rotation. For details of the irradiation procedure and the standards used, see [17] and Table S1.

### 4.2. Noble Gas Mass Spectrometry

Noble gas isotopes of irradiated mineral separates were determined using a ThermoFisher ARGUS VI mass spectrometer [10]. Noble gases were released by both $CO_2$ laser step heating and in vacuo crushing. For the procedure followed for gas extraction by laser step heating, see details in [17]. In vacuo crushing was performed using screw-operated crushers constructed from modified Nupro® valves [85]. Samples are crushed in disposable stainless-steel containers by repeated closure of the valve between 1 and 15 times to ensure efficient gas release from fluid inclusions. Extracted noble gases were then purified and isotopically analysed using the same procedures for laser heating.

Blanks were determined at multiple times to check the background of the spectrometers. Average blanks were $7.52 \times 10^{-11}$ cm³ STP $^{40}$Ar and $6.16 \times 10^{-19}$ cm³ STP $^{129}$Xe, with Kr blanks being below detection. Calibrations, using known amounts of atmospheric noble gases, were carried out daily to determine mass discrimination for Ar isotopes, and the instrument sensitivity for Ar, Kr and Xe isotopes. Raw data were corrected for blanks, radioactive decay (39 Ar), mass discrimination (36–39 Ar) and neutron interferences (Ar isotopes). Parent element concentrations were determined using mass spectrometer sensitivity and irradiation standards as detailed in [10].

### 4.3. Time-of-Flight Secondary Ion Mass Spectrometry (TOF-SIMS)

Halogen distributions within grains and at grain boundaries were mapped using TOF-SIMS with the IDLE 3 instrument [86]. The IDLE 3 instrument is equipped with a multi-channel plate detector, followed by a scintillator and a photomultiplier. The details of the TOF-SIMS and IDLE 3 setup, and the procedure followed for measuring halogens in samples, are described in [17]. Detection limits were 92 ± 73 ppm for F, 307 ± 183 ppm for Cl and 38 ± 55 ppm for Br (background ± 3SD), based on analyses of the halogen-free San Carlos olivine.

### 4.4. Electron-Probe Micro-Analysis (EPMA)

Analysis of Si, Al, Fe, Ca, Na, Mg, K, Ti, Mn, Cr, Ni, P, F and Cl was carried out at the University of Manchester with a Cameca SX100 electron microprobe, using wavelength dispersive spectrometry (WDS). Operating conditions were 15 kV

accelerating voltage with a 20 nA beam current, de-focused to 20 μm spot size. Counting was conducted on Kα lines for all elements, with 20 s count times for Si, Fe, Mg, Al, Ca, K, Na, Mn, Cr, Ni, P, Ti, and 60 s count time for Cl and F. A PC0 diffraction crystal was used for the analysis of F to enhance both peak resolution and total counts. During standardisation and analysis, time-zero regression was performed for F, Cl, Na and K to account for any decrease in count rates with time due to element migration. Using this setup, detection limits were ~80 ppm for Cl and ~400 ppm for F. Quantification standards used were wollastonite (Si, Ca), corundum (Al), fayalite (Fe), jadeite (Na), periclase (Mg), K-feldspar (K), rutile (Ti), tephroite (Mn), $Cr_2O_3$ (Cr), NiO (Ni), fluorapatite (P, F) and sodium chloride (Cl). Mineral formulae were re-calculated using the following number of oxygen atoms: olivine 4(O); pyroxene 6(O); garnet 12(O); feldspar 8(O); quartz 2(O); amphibole 23(O); calcite 3(O); mica 11(O); magnetite 1(O); apatite 13(O); rutile 2(O); clinohumite 17(O). The $H_2O$ content of hydrous minerals was assumed by difference.

### 4.5. Raman Spectroscopy

Raman spectra were acquired using a Horiba XploRA PLUS spectrometer equipped with an electron-multiplying charge-coupled device (EMCCD) detector. A solid-state laser, set at a wavelength of 532 or 785 nm, was used to excite Raman scattering. Raman spectra were obtained by averaging 5 spectra acquired with a count time of 20 s, for shift ranges 200–1200 $cm^{-1}$ (aluminosilicate framework domain), 1200–3000 $cm^{-1}$ ($CO_2$, $H_2O$, $N_2$ and $CH_4$) and 3000–4000 $cm^{-1}$ (OH stretching domain), relative to the wavelength of the laser.

### 4.6. Microthermometry

Fluid inclusions were analysed on a Linkam THMS600 heating-freezing stage. The apparent salinities of fluids in samples, expressed as wt% NaCl, were calculated from the freezing point depression relationships of the $H_2O$-NaCl system [87]. The analytical precision is ± 0.1 °C between −30 and +20 °C.

### 4.7. Bulk Rock Calculations

The bulk chemistry—major elements, F and Cl—of samples was calculated from the major element and halogen data of individual mineral phases determined by EPMA, along with the modal mineral abundances in samples. Calculated bulk rock chemistries do not include all accessory phases present within samples, but accessory phases are not expected to significantly alter major element chemistry. Calculated bulk rock chemistries here are similar to XRF data obtained from eclogites and websterites in other studies of the WGR [60,63]. Bulk rock calculations of F and Cl do not include the halogen contents of mineral inclusions analysed by EPMA. As it is not feasible to analyse every inclusion within each sample, nor accurate to assume the F and Cl content of inclusions that were analysed is representative, including them will likely lead to spurious results. Therefore, the calculated bulk F and Cl content of samples will be a slight underestimate. However, it is noted that the abundances of these elements obtained here are similar to those reported in other studies of the WGR [60].

## 5. Results

The full datasets for major element data, modal mineral abundances, secondary ion maps and halogen concentrations and ratios measured in samples by EPMA, TOF-SIMS and NI-NGMS are presented in Supplementary Material Tables S2-S7.

### 5.1. Bulk Rock Chemistry

The bulk rock chemistry—major elements and F and Cl—of Årsheimneset and Svartberget, as calculated by EPMA analysis and modal mineral abundances (Supplementary Material Table S5), is presented in Table 2. The high Fe and Ti contents

of some eclogites suggests that they had gabbroic or granulitic precursors. Figure 5 shows that the bulk rock halogen content is generally higher in samples from Årsheimneset than samples from Svartberget.

a)



b)
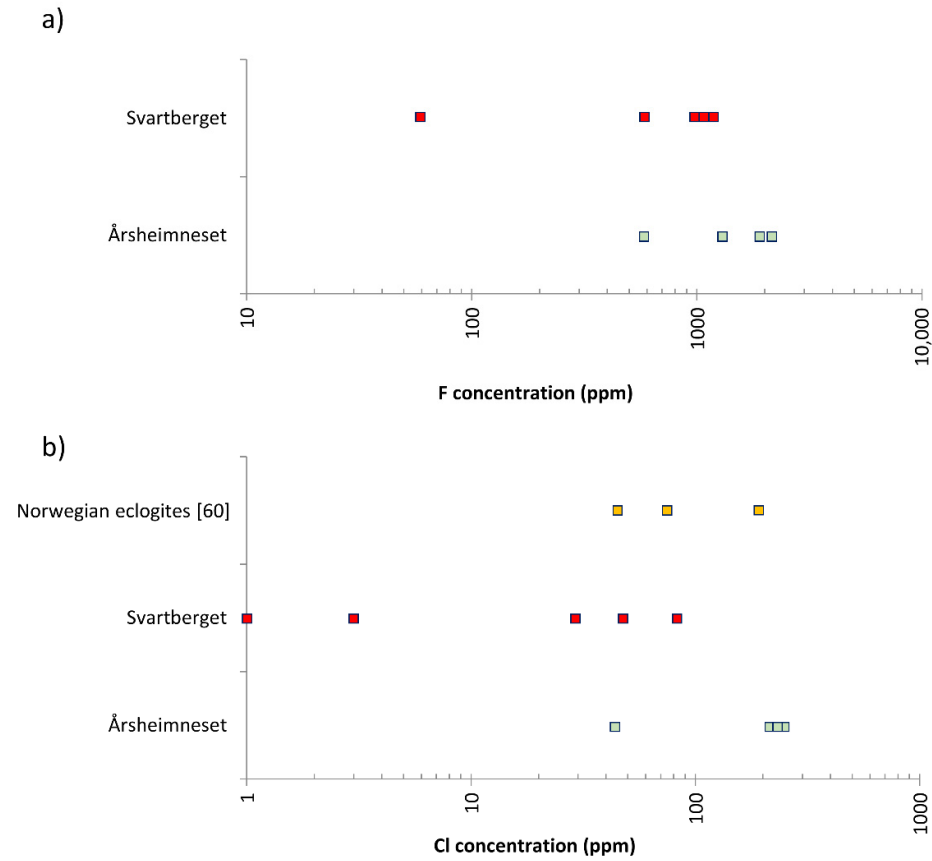


**Figure 5.** Comparison of bulk rock F (**a**) and Cl (**b**) ranges between Årsheimneset, Svartberget and the data of [60].

**Table 2.** Bulk rock data (major elements and F and Cl) for WGR samples, calculated using EPMA data and modal mineral abundances. Abbreviations are: A.—Årsheimneset and S.—Svartberget.

| Sample | QC26C | QC26E | QC26G | QC26H | QC36A | QC36C | QC36D | QC36G | QC36U |
|---|---|---|---|---|---|---|---|---|---|
| Locality | A. | A. | A. | A. | S. | S. | S. | S. | S. |
| Lithology | Gneiss | Eclogite | Websterite | Websterite | Websterite | Peridotite | Websterite | Websterite | Garnetite |
| $SiO_2$ | 74.97 | 49.56 | 44.07 | 52.16 | 49.71 | 43.50 | 50.33 | 44.86 | 41.79 |
| $TiO_2$ | 0.02 | 2.01 | 2.26 | 3.16 | 0.09 | 0.22 | 0.19 | 1.36 | 0.09 |
| $Al_2O_3$ | 12.05 | 9.66 | 9.24 | 9.16 | 3.44 | 2.95 | 6.48 | 12.95 | 14.19 |
| $Cr_2O_3$ | - | 0.07 | 0.22 | 0.23 | 0.27 | 0.24 | 0.39 | 0.25 | 0.11 |
| FeO | 2.83 | 10.87 | 10.93 | 10.76 | 10.89 | 13.13 | 8.00 | 9.98 | 11.51 |
| MnO | 3.44 | 0.17 | 0.18 | 0.27 | 0.23 | 0.23 | 0.24 | 0.39 | 0.51 |
| MgO | 0.36 | 9.01 | 14.75 | 12.34 | 26.39 | 35.16 | 18.08 | 13.45 | 17.01 |
| CaO | 1.71 | 13.65 | 10.91 | 7.44 | 7.77 | 4.07 | 10.70 | 9.06 | 8.61 |
| $Na_2O$ | 3.90 | 1.71 | 1.13 | 1.37 | 0.21 | 0.07 | 1.29 | 1.72 | 0.22 |
| $K_2O$ | 0.70 | 0.01 | 1.43 | 1.25 | 0.03 | 0.01 | 0.98 | 1.69 | 1.24 |
| $P_2O_5$ | 0.82 | 2.47 | - | 0.41 | 0.01 | - | - | - | 2.35 |
| **Total** | **100.80** | **99.19** | **95.14** | **98.56** | **99.04** | **99.58** | **96.64** | **95.71** | **97.64** |
| F (ppm) | 576 | 1228 | 2126 | 1960 | 59 | 1195 | 582 | 1001 | 1094 |
| Cl (ppm) | 44 | 250 | 222 | 237 | 3 | 1 | 29 | 48 | 81 |
| F/Cl (wt) | 13 | 5 | 10 | 8 | 20 | 1195 | 20 | 21 | 14 |

### 5.2. Fluorine and Chlorine in Hydrous Mineral Phases

The average chemical compositions of amphibole, apatite, biotite, clinohumite and phengite are presented in Table 3. The full range of EPMA data can be found in Supplementary Tables S6 and S7. Figure 6 shows the average ranges in F/Cl ratios of hydrous mineral phases.
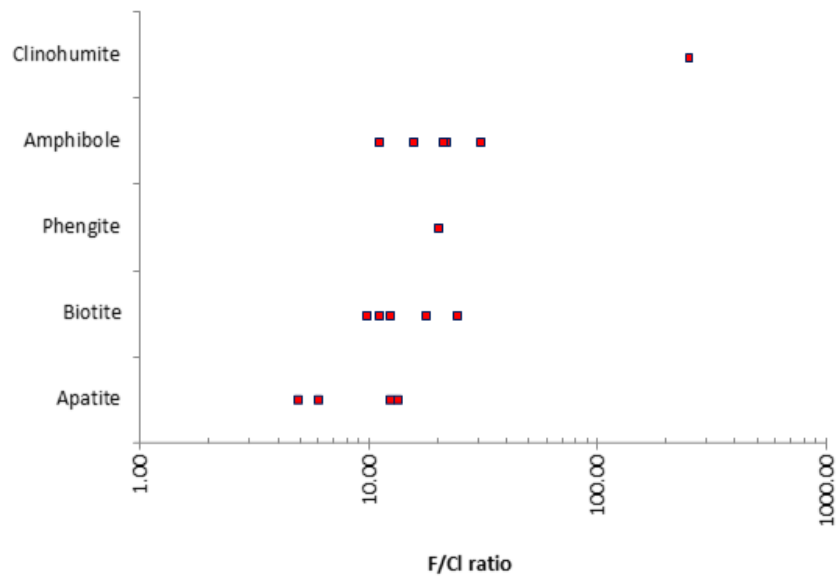


**Figure 6.** Comparison of the F/Cl ratios of eclogitic hydrous minerals.

Apatites from samples QC26C, QC26E, QC26H and QC36U are predominantly of the fluorapatite variety (Table 3), with up to 2.8 wt% F (0.77 F atomic formula units, a.f.u.) and <0.5 wt% Cl (0.06 Cl a.f.u.). The F/Cl ratios of apatite samples ranges from 5 to 13, with an average value of 9.

Amphibole inclusions within garnet contain more Cl (up to 2 wt%) than matrix amphibole (up to 0.25 wt%), whereas matrix amphibole contains more F (average 0.3 wt%) than amphibole inclusions (average 0.2 wt%). Amphibole inclusions in garnet have an average F/Cl ratio of ~0.3, whereas matrix amphibole has an average F/Cl ratio of ~20 (Table 3). Silicon is positively correlated with both F ($R^2$ = 0.95) and Cl ($R^2$ = 0.56). Aluminium is negatively correlated with F ($R^2$ = −0.76) but shows no correlation with Cl ($R^2$ = −0.28).

Biotite is common in samples but is more abundant in samples from Svartberget than Årsheimneset (Figure 2). In eclogite and websterite they tend to be Ti-phlogopite but in felsic rocks are more Fe rich and less Ti rich. Biotites from Årsheimneset and Svartberget are F rich, with up to 1.3 wt% F and 0.12 wt% Cl (Table 3). Biotite inclusions in garnet have similar F content (~1 wt%) and Cl contents (~0.1 wt%) to matrix biotite. F/Cl ratios in matrix biotite range from 10 to 24, with an average F/Cl of 17. Aluminium correlates negatively with both F ($R^2$ = −0.89) and Cl ($R^2$ = −0.96).

Clinohumite from peridotite sample QC36C is predominantly fluorine and titanium rich, with 2.39 wt% F and 3.03 wt% Ti (Table 3). The F/Cl ratio of clinohumite is the highest of all hydrous mineral phases analysed, at ~240. A slight negative correlation exists between Ti and F ($R^2$ = −0.54).

White mica from sample QC26C, like other hydrous mineral phases, is predominantly F-bearing relative to Cl, with an F content of 0.2 wt% and a Cl content of 0.01 wt%. The F/Cl ratio is 20 (Table 3). There is no apparent correlation between halogen (F, Cl) and other elements in white mica.

**Table 3.** Hydrous mineral compositions obtained by EPMA.

| Mineral | Ap | Ap | Ap | Ap | Amp | Amp | Amp | Amp | Amp | Amp | Bt | Bt | Bt | Bt | Bt | Chu | Ph |
|---|---|---|---|---|---|---|---|---|---|---|---|---|---|---|---|---|---|
| Sample | QC26C | QC26E | QC26H | QC36U | QC26G | QC26H | QC36A | QC36D | QC36G | QC36U | QC26G | QC26H | QC36D | QC36G | QC36U | QC36C | QC26C |
| $SiO_2$ | 0.04 | 0.07 | 0.03 | 0.10 | 53.57 | 53.95 | 44.61 | 46.35 | 46.83 | 44.22 | 40.35 | 40.80 | 37.57 | 38.24 | 39.48 | 35.89 | 46.49 |
| $TiO_2$ | - | - | - | - | 0.12 | 0.07 | 0.29 | 0.16 | 0.23 | 0.14 | 1.70 | 1.34 | 1.08 | 1.76 | 0.40 | 3.03 | 0.34 |
| $Al_2O_3$ | 0.01 | 0.08 | - | 0.03 | 3.59 | 3.22 | 12.12 | 4.69 | 10.02 | 12.18 | 13.61 | 13.11 | 15.22 | 15.85 | 15.47 | - | 30.85 |
| $Cr_2O_3$ | - | - | - | - | 0.12 | 0.16 | 0.33 | 0.27 | 0.13 | 0.36 | 0.15 | 0.18 | 0.45 | 0.14 | 0.21 | - | 0.01 |
| FeO | 0.08 | 0.15 | 0.07 | 0.12 | 7.44 | 7.94 | 6.61 | 4.78 | 8.84 | 8.03 | 7.21 | 7.96 | 6.74 | 9.11 | 6.77 | 10.68 | 3.17 |
| MnO | 0.00 | 0.01 | 0.02 | 0.04 | 0.07 | 0.11 | 0.08 | 0.11 | 0.22 | 0.16 | 0.01 | 0.02 | 0.02 | 0.07 | 0.03 | 0.15 | 0.08 |
| MgO | 0.04 | 0.08 | 0.03 | 0.19 | 18.93 | 19.74 | 17.19 | 17.73 | 16.13 | 15.72 | 20.69 | 20.86 | 19.48 | 18.88 | 21.26 | 47.03 | 1.64 |
| CaO | 54.20 | 53.99 | 53.95 | 53.88 | 10.75 | 9.09 | 12.11 | 7.75 | 10.47 | 11.78 | 0.02 | 0.01 | −0.01 | −0.02 | 0.06 | 0.01 | −0.01 |
| $Na_2O$ | 0.08 | 0.18 | 0.10 | 0.05 | 1.07 | 1.22 | 1.97 | 1.18 | 2.27 | 1.93 | 0.89 | 0.50 | 0.52 | 0.77 | 0.53 | 0.03 | 0.46 |
| $K_2O$ | 0.00 | 0.01 | 0.01 | - | 0.47 | 0.44 | 0.89 | 0.39 | 0.38 | 0.81 | 7.80 | 8.84 | 6.84 | 8.77 | 8.19 | 0.01 | 10.27 |
| $P_2O_5$ | 41.08 | 41.32 | 41.69 | 39.17 | - | - | - | - | - | - | - | - | - | - | - | 0.01 | - |
| F | 2.29 | 2.05 | 2.76 | 1.18 | 0.44 | 0.53 | 0.20 | 0.27 | 0.30 | 0.16 | 1.08 | 1.31 | 0.36 | 0.48 | 0.24 | 2.39 | 0.20 |
| Cl | 0.19 | 0.42 | 0.43 | 0.09 | 0.04 | 0.24 | 0.01 | 0.00 | 0.01 | 0.01 | 0.11 | 0.12 | 0.02 | 0.02 | 0.02 | 0.01 | 0.01 |
| Total | 95.51 | 95.87 | 95.88 | 93.57 | 96.12 | 95.91 | 96.21 | 83.40 | 95.50 | 95.33 | 92.44 | 93.62 | 87.91 | 93.56 | 92.41 | 96.84 | 93.30 |
| O:F-Cl | 1.00 | 1.01 | 1.25 | 0.52 | 0.19 | 0.28 | 0.09 | 0.11 | 0.13 | 0.07 | 0.48 | 0.58 | 0.16 | 0.21 | 0.11 | 1.00 | 0.09 |
| F/Cl | 12 | 5 | 6.5 | 13 | 11 | 21 | 21 | - | 30 | 16 | 10 | 22 | 18 | 24 | 12 | 240 | 20 |
| **Total** | **94.51** | **94.86** | **94.63** | **93.05** | **95.93** | **95.63** | **96.12** | **83.29** | **95.37** | **95.26** | **91.96** | **93.04** | **87.75** | **93.35** | **92.30** | **95.84** | **93.21** |
| Si | 0.01 | 0.01 | - | 0.01 | 7.65 | 7.70 | 6.46 | 7.52 | 6.85 | 6.51 | 2.96 | 2.98 | 2.89 | 2.84 | 2.89 | 3.92 | 3.18 |
| Ti | - | - | - | - | 0.01 | 0.01 | 0.03 | 0.02 | 0.03 | 0.02 | 0.09 | 0.07 | 0.06 | 0.10 | 0.02 | 0.25 | 0.02 |
| Al | - | - | - | - | 0.60 | 0.54 | 2.07 | 0.90 | 1.73 | 2.11 | 1.17 | 1.13 | 1.38 | 1.38 | 1.34 | - | 2.50 |
| Cr | - | - | - | - | 0.01 | 0.02 | 0.04 | 0.04 | 0.02 | 0.04 | - | - | - | - | - | - | - |
| $Fe^{2+}$ | 0.01 | 0.01 | 0.01 | 0.01 | 0.90 | 0.96 | 0.61 | 0.66 | 1.09 | 0.91 | 0.44 | 0.49 | 0.43 | 0.56 | 0.42 | 0.98 | 0.18 |
| Mn | - | - | - | - | 0.01 | 0.01 | 0.01 | 0.02 | 0.03 | 0.02 | 0.01 | 0.01 | 0.01 | 0.01 | 0.01 | 0.01 | 0.01 |
| Mg | - | 0.01 | - | 0.02 | 4.03 | 4.19 | 3.71 | 4.29 | 3.52 | 3.45 | 2.26 | 2.27 | 2.23 | 2.07 | 2.32 | 7.66 | 0.17 |
| Ca | 5.07 | 5.04 | 4.98 | 5.25 | 1.64 | 1.39 | 1.88 | 1.35 | 1.64 | 1.85 | - | - | - | - | 0.01 | - | - |
| Na | 0.02 | 0.03 | 0.02 | 0.01 | 0.30 | 0.34 | 0.55 | 0.37 | 0.64 | 0.55 | 0.13 | 0.07 | 0.08 | 0.11 | 0.08 | 0.01 | 0.06 |
| K | - | - | - | - | 0.09 | 0.08 | 0.16 | 0.08 | 0.07 | 0.15 | 0.74 | 0.84 | 0.70 | 0.83 | 0.78 | - | 0.91 |
| P | 3.03 | 3.05 | 3.04 | 3.02 | - | - | - | - | - | - | - | - | - | - | - | - | - |
| F | 0.63 | 0.56 | 0.75 | 0.34 | 0.20 | 0.24 | 0.09 | 0.14 | 0.14 | 0.08 | 0.25 | 0.30 | 0.09 | 0.05 | 0.06 | 0.41 | 0.04 |
| Cl | 0.03 | 0.06 | 0.19 | 0.01 | 0.01 | 0.05 | 0.002 | 0.00 | 0.00 | 0.002 | 0.01 | 0.02 | 0.003 | 0.002 | 0.002 | 0.00 | 0.001 |
| **Total** | **8.12** | **8.15** | **8.05** | **8.31** | **15.23** | **15.24** | **15.52** | **15.23** | **15.61** | **15.70** | **7.80** | **7.84** | **7.74** | **7.86** | **7.84** | **12.83** | **7.02** |

Abbreviations: Amp—amphibole, Ap—apatite, Bt—biotite, Chu—clinohumite, and Ph—phengite.

### 5.3. NI-NGMS Halogens

The concentrations of halogens and potassium obtained by crushing and step heating analyses of Årsheimneset and Svartberget are presented in Tables 4 and 5. Overall, concentrations of halogens vary widely, with ranges in Cl from 0.1 to 1014 ppm, Br from 2.7 to 2116 ppb and I from 0.03 to 12.1 ppb. The K/Cl ratios of samples (exc. micas) range from 0.9 to 237. Crushing analyses yielded Cl contents from 0.1 to 11.5 ppm, Br from 2.7 to 166 ppb and I from 0.03 to 1.02 ppb. Heating analyses yielded Cl contents from 0.6 to 1014 ppm, Br from 8.7 to 2116 ppb and I from 0.1 to 12.1 ppb. A comparison between halogens released by individual crushing and heating analyses of separates is shown in Figure S1a–c of the appendix. Crushing experiments released 2–58% of the total Cl content, 7–64% of the total Br content and 8–87% of the total iodine content. Overall, approximately 30% of the total halogen content is released by crushing, with crushing releasing a larger proportion of the total halogen content in the order Cl < Br < I. During

heating analyses, biotite contains the highest concentrations of halogens on average, with up to 1000 ppm Cl, 1100 ppb Br and 12 ppb I, followed by phengite, with up to 50 ppm Cl, 270 ppb Br and 5 ppb I. Garnet contains the lowest halogen abundances, with 0.7 ppm Cl, 8.8 ppb Br and 0.15 ppb I. However, garnet also shows the largest range in halogen abundances, from 0.7 to 407 ppm Cl, 8.8 to 2100 ppb Br and 0.15 to 4.4 ppb I. Quartz and olivine separates have halogen abundances intermediate between garnet and biotite, with 3–14 ppm and 6 ppm Cl, respectively, 60–220 ppb and 63 ppb Br, respectively and 0.15–0.75 ppb and 0.38 ppb I, respectively. Figure 7a–c shows the individual crushing and heating analyses as a comparison between mineral phase and area. Figure S1d–f compares combined heating and crushing analyses, i.e., total halogen content of separates between the Årsheimneset and Svartberget localities. Overall, halogen abundances in both Årsheimneset and Svartberget separates cover a similar range. However, a bimodal abundance pattern at Svartberget is caused by Cl-, Br- and I-rich biotite, such that, on average, mineral separates at Årsheimneset are more halogen rich, which matches the F and Cl abundances obtained by EPMA (Figure 5). In addition, crushing released on average more halogen content in Årsheimneset samples—27% Cl, 32% Br and 40% I—than in Svartberget samples—19% Cl, 20% Br and 30% I. Little variation exists between rock type and halogen content, with the exception being olivine websterite, which shows elevated concentrations of I, relative to Cl and Br abundances (Figure S1g–i).
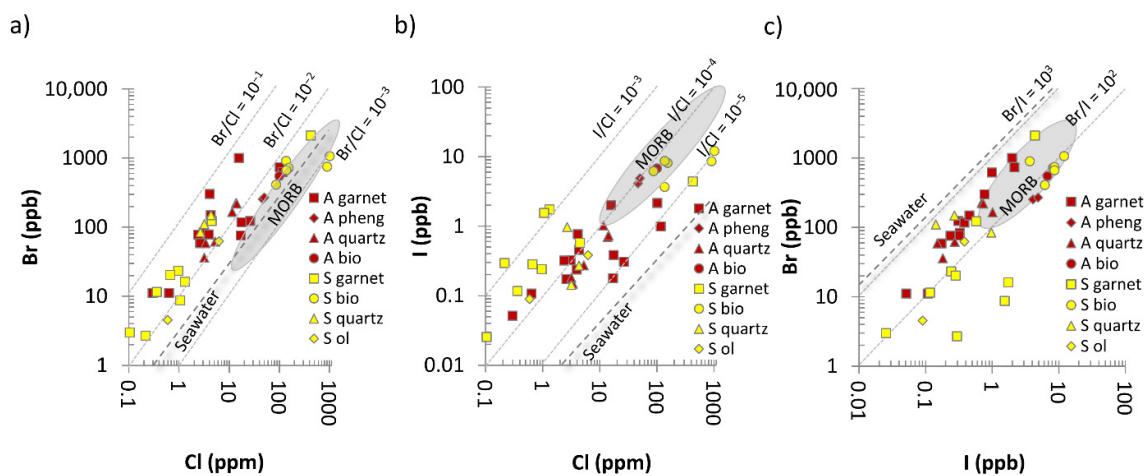


**Figure 7.** The Br/Cl (**a**), I/Cl (**b**) and Br/I (**c**) ratios of Årsheimneset and Svartberget separates, along with MORB, seawater and constant halogen ratio values. MORB fields from [8,12,88]. See Figure S1 in the Supplementary Material for an extension to this figure that includes several further plots.

The relationships between Br/Cl, I/Cl and Br/I ratios of samples are shown in Figures 7 and 8, along with published halogen data for seawater, MORB, pore fluids, Alpine eclogites and garnet peridotites [8,12,17,18,88–93]. The Br/Cl ratios obtained by crushing and heating show a wide range, spanning two orders of magnitude from $8.24 \times 10^{-4}$ to $8.60 \times 10^{-2}$. I/Cl ratios show a similarly wide range, from $8.48 \times 10^{-6}$ to $1.55 \times 10^{-3}$. Despite the overall wide ranges, Figure S1a–c shows that there is a relatively small difference in the ranges of Br/Cl, I/Cl and Br/I ratios released by heating and crushing. Figures 7 and S1 show that there is little correlation overall of Br/Cl and I/Cl between crushing vs. heating, area, mineral type and rock type. In contrast Br/I ratios, with the exception of a couple of data points corresponding to the I-rich sample QC36A, are well-correlated (Figures 7c and S1c,f,i).

**Table 4.** Halogen and K abundances and ratios obtained by crushing and heating analyses of Årsheimneset samples (C = crushing; F = fusion).

| Sample | Cl (ppm) | Br (ppb) | I (ppb) | Br/Cl ($\times 10^{-2}$) | I/Cl ($\times 10^{-4}$) | Br/I ($10^2$) | K (ppm) | K/Cl |
|---|---|---|---|---|---|---|---|---|
| QC26C-Grt (F) | 15.7 | 1005.4 | 2.00 | 6.42 | 1.28 | 5.02 | 1068 | 68.2 |
| QC26C-Grt (C) | 4.1 | 301.3 | 0.78 | 7.36 | 1.87 | 3.93 | 17 | 4.2 |
| **QC26C-Grt total** | **19.8** | **1306.7** | **2.78** | **6.62** | **1.41** | **4.70** | **1085** | **54.9** |
| QC26C-Ph-1 (F) | 40.6 | 253.8 | 4.11 | 0.55 | 0.88 | 0.62 | 89,209 | 2197 |
| QC26C-Ph-2 (F) | 50.2 | 269.5 | 4.90 | 0.54 | 0.98 | 0.55 | 80,764 | 1609 |
| QC26E-Grt-1 (F) | 17.5 | 117.4 | 0.38 | 0.67 | 0.22 | 3.06 | 23 | 1.3 |
| QC26E-Grt-1 (C) | 0.3 | 11.2 | 0.05 | 3.78 | 1.74 | 2.17 | 1 | 3.3 |
| **QC26E-Grt-1 total** | **17.8** | **128.6** | **0.43** | **0.72** | **0.24** | **2.99** | **24** | **1.3** |
| QC26E-Grt-2 (F) | 26.3 | 123.4 | 0.31 | 0.47 | 0.12 | 4.01 | 25 | 0.9 |
| QC26E-Qz-1 (F) | 5.3 | 61.9 | 0.27 | 1.17 | 0.52 | 2.26 | 21 | 4.0 |
| QC26E-Qz-1 (C) | 3.2 | 36.2 | 0.18 | 1.15 | 0.57 | 2.00 | 6 | 1.9 |
| **QC26E-Qz-1 total** | **8.5** | **98.1** | **0.45** | **1.16** | **0.53** | **2.18** | **27** | **3.2** |
| QC26E-Qz-2 (F) | 3.4 | 58.6 | 0.15 | 1.75 | 0.47 | 3.92 | 12 | 3.6 |
| QC26G-Grt-1 (F) | 3.1 | 83.8 | 0.32 | 2.72 | 1.06 | 2.58 | 53 | 17.3 |
| QC26G-Grt-1 (C) | 4.3 | 148.8 | 0.46 | 3.46 | 1.06 | 3.25 | 10 | 2.3 |
| **QC26G-Grt-1 total** | **7.4** | **232.6** | **0.78** | **3.16** | **1.06** | **2.98** | **63** | **8.5** |
| QC26G-Grt-2 (F) | 101.5 | 733.8 | 2.16 | 0.73 | 0.21 | 3.39 | 682 | 6.7 |
| QC26G-Grt-2 (C) | 0.8 | 29.2 | 0.13 | 3.51 | 1.51 | 2.33 | 12 | 14.5 |

| | | | | | | | | |
|---|---|---|---|---|---|---|---|---|
| ***QC26G-Grt-2 total*** | **102.3** | **763.0** | **2.29** | **0.75** | **0.22** | **3.33** | **694** | **6.8** |
| *QC26G-Grt-2a (C)* | 1.6 | 47.9 | 0.19 | 3.07 | 1.24 | 2.47 | 7 | 4.5 |
| *QC26G-Grt-3 (F)* | 2.6 | 59.0 | 0.17 | 2.26 | 0.65 | 3.40 | 64 | 24.5 |
| *QC26G-Grt-3 (C)* | 0.6 | 11.2 | 0.11 | 1.77 | 1.69 | 1.04 | 2.9 | 4.6 |
| ***QC26G-Grt-3 total*** | **3.2** | **70.2** | **0.28** | **2.17** | **0.86** | **2.51** | **66.9** | **20.6** |
| *QC26H-Qz-1 (F)* | 13.7 | 224.4 | 0.69 | 1.64 | 0.51 | 3.23 | 38.9 | 2.8 |
| *QC26H-Qz-1 (C)* | 11.5 | 166.1 | 1.02 | 1.45 | 0.86 | 1.63 | 23 | 2.0 |
| ***QC26H-Qz-1 total*** | **25.2** | **390.5** | **1.71** | **1.55** | **0.68** | **2.28** | **61.9** | **2.5** |
| *QC26H-Qz-2 (F)* | 14.2 | 220.1 | 0.73 | 1.55 | 0.52 | 3.00 | 78 | 5.5 |
| *QC26H-Grt-1 (F)* | 116.8 | 622.9 | 0.99 | 0.53 | 0.08 | 6.30 | 185 | 1.6 |
| *QC26H-Grt-1 (C)* | 3.9 | 78.5 | 0.24 | 1.99 | 0.60 | 3.30 | 8.6 | 2.2 |
| ***QC26H-Grt-1 total*** | **120.7** | **701.4** | **1.23** | **0.58** | **0.10** | **5.70** | **193.6** | **1.6** |
| *QC26H-Grt-2 (F)* | 17.1 | 75.8 | 0.18 | 0.44 | 0.10 | 4.26 | 33 | 1.9 |
| *QC26H-Bt (F)* | 99.5 | 548.8 | 6.79 | 0.55 | 0.68 | 8.08 | 71,810 | 721 |

**Table 5.** Halogen and K abundances and ratios obtained by crushing and heating analyses of Svartberget samples.

| *Sample* | *Cl* (ppm) | *Br* (ppb) | *I* (ppb) | *Br/Cl* (×10⁻²) | *I/Cl* (x10⁻⁴) | *Br/I* (10²) | *K* (ppm) | *K/Cl* |
|---|---|---|---|---|---|---|---|---|
| QC36A-Ol (F) | 6.2 | 62.9 | 0.38 | 1.01 | 0.62 | 1.64 | 21 | 3.4 |
| QC36A-Ol (C) | 0.6 | 4.6 | 0.09 | 0.77 | 1.52 | 5.07 | 2 | 3.4 |
| **QC36A-Ol total** | **6.8** | **67.5** | **0.47** | **0.99** | **0.69** | **1.44** | **23** | **3.4** |
| QC36A-Grt-1 (F) | 1.3 | 16.2 | 1.74 | 1.23 | 13.0 | 0.09 | 47 | 35.6 |
| QC36A-Grt-1 (C) | 0.2 | 2.7 | 0.29 | 1.26 | 14.0 | 0.09 | 13 | 61.9 |
| **QC36A-Grt-1 total** | **1.5** | **18.9** | **2.03** | **1.24** | **13.3** | **0.09** | **60** | **39.2** |
| QC36A-Grt-2 (F) | 1.1 | 8.8 | 1.55 | 0.83 | 15.0 | 0.06 | 22 | 20.9 |
| QC36D-Grt-1 (F) | 1.0 | 23.4 | 0.24 | 2.44 | 2.52 | 0.97 | 129 | 134 |
| QC36D-Grt-1 (C) | 0.1 | 3.0 | 0.03 | 2.88 | 3.00 | 1.18 | 1 | 10.0 |
| **QC36D-Grt-1 total** | **1.1** | **26.4** | **0.27** | **2.49** | **2.55** | **0.98** | **130** | **122** |
| QC36D-Grt-2 (F) | 0.7 | 20.3 | 0.28 | 3.06 | 4.25 | 0.72 | 94 | 142 |
| QC36D-Bt-1 (F) | 136.7 | 904.8 | 3.65 | 0.66 | 0.27 | 2.48 | 70240 | 513 |
| QC36D-Bt-2 (F) | 152.9 | 720.5 | 8.19 | 0.47 | 0.54 | 0.88 | 76495 | 500 |
| QC36G-Grt-1 (F) | 4.5 | 123.3 | 0.58 | 2.75 | 1.29 | 2.14 | 1065 | 237 |
| QC36G-Grt-1 (C) | 0.4 | 11.5 | 0.12 | 3.20 | 3.24 | 0.99 | 3 | 8.3 |
| **QC36G-Grt-1 total** | **4.9** | **134.8** | **0.7** | **2.79** | **1.45** | **1.93** | **1068** | **220** |
| QC36G-Grt-2 (F) | 427.1 | 2116.1 | 4.38 | 0.50 | 0.10 | 4.83 | 1094 | 2.6 |
| QC36G-Bt-1 (F) | 906.0 | 747.0 | 8.60 | 0.08 | 0.09 | 0.87 | 77912 | 86.0 |
| QC36G-Bt-2 (F) | 1014.1 | 1069.8 | 12.09 | 0.11 | 0.12 | 0.86 | 81807 | 81 |

| | | | | | | | |
|---|---|---|---|---|---|---|---|
| *QC36G-Bt-3 (F)* | 86.5 | 410.4 | 6.16 | 0.48 | 0.71 | 0.67 | 40906 | 473 |
| *QC36G-Bt-4 (F)* | 137.5 | 668.8 | 8.66 | 0.49 | 0.63 | 0.77 | 83836 | 610 |
| *QC36Q-Qz-1 (F)* | 4.3 | 148.7 | 0.27 | 3.45 | 0.63 | 5.50 | 556 | 129 |
| *QC36Q-Qz-1 (C)* | 3.2 | 36.2 | 0.18 | 1.14 | 0.57 | 2.00 | 6 | 1.9 |
| ***QC36Q-Qz-1 total*** | **7.5** | **184.9** | **0.45** | **2.47** | **0.60** | **4.11** | **562** | **75** |
| *QC36Q-Qz-2 (F)* | 3.2 | 109.9 | 0.14 | 3.47 | 0.45 | 7.70 | 18 | 5.7 |

Figure 8a shows that the halogen ratios from individual crushing and heating analyses show a large degree of overlap, and plot within a Br-enriched region of the halogen mixing plot. Figure 8b compares combined crushing and heating halogen data for mineral types against published data for other rocks and fluids (see figure caption for details). Figure 8b indicates that, excluding one biotite sample (QC36G), the Br/Cl and I/Cl ratios of Årsheimneset and Svartberget separates are close to or higher than modern seawater and follow a rough trend of increasing Br/Cl and I/Cl ratios. Figure 8c shows combined crushing and heating analyses of mineral types and area and shows that the Br/Cl and I/Cl ratios of Årsheimneset and Svartberget samples are distinct from MORB, marine pore fluids and Alpine eclogites and garnet peridotites but lie in a similar region to Precambrian saline groundwaters from the Stripa granite and Canadian shield. Figure 8c also shows that the Br/Cl and I/Cl ratios of Årsheimneset and Svartberget samples follow a mixing trend defined by seawater and an unknown Br- and I-rich endmember. This endmember has a composition similar to that observed in some diamonds and mantle xenoliths [21,94].
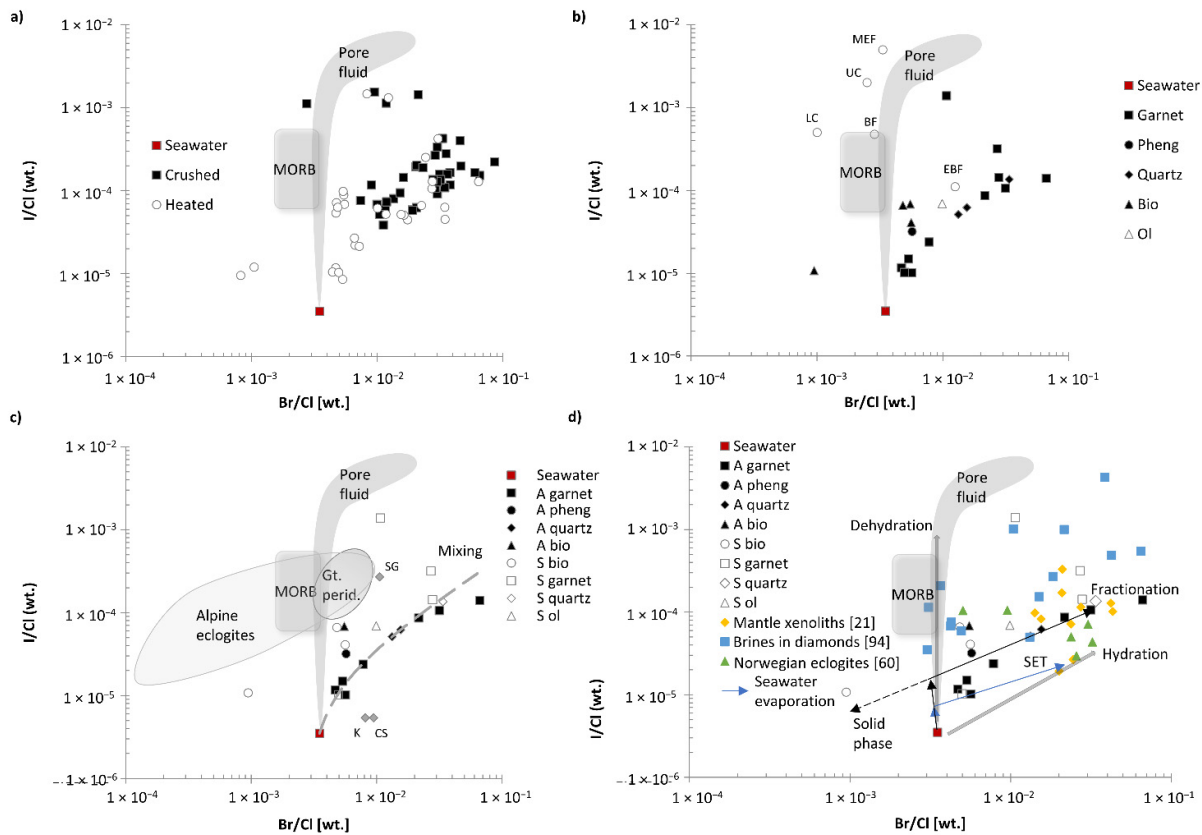
**Figure 8.** I/Cl vs. Br/Cl ratios of WGR samples. (**a**) Crushing vs. heating compared to MORB, seawater and pore fluid fields. (**b**) Mineral type compared to MORB, seawater, pore fluid, Monviso eclogite fluids (MEF), upper crust (UC), lower crust (LC), sedimentary basin fluids (BF) and evaporite-bearing fluids (EBF). (**c**) Mineral phase and area compared to fields of MORB, marine pore fluid, Alpine eclogites, garnet peridotites, the seawater halogen composition and the composition of crustal basement fluids from the Stripa granite (SG), the Keeweenaw peninsula (K) and the Canadian shield (CS). The dotted line represents a mixing trend, according to the mixing equation in [95], between seawater and an unknown Br- and I-rich endmember, and shows that many of the samples in this study lie along or close to the mixing trend, (**d**) Mineral type and area compared to MORB, seawater, pore fluid, Norwegian eclogites [60], brines in diamonds [94] and Siberian xenoliths [21] from the sub-continental lithospheric mantle. Additionally, shown in (**d**) are a fractionation trend through preferential Cl removal and a seawater evaporation trend (SET), along with the evolution of halogen ratios through metamorphic processes such as dehydration and hydration reactions [60]. MORB field is from [8,12,88]; Seawater is from [89]. Pore fluids are from [90–93]. MEF is from [96], UC and LC are from [97], BF is from [98], EBF is from [60], the Stripa granite is from [99], the Keeweenaw peninsula is from [100] and the Canadian shield is from [101].

### 5.4. Halogen Distribution

Secondary ion maps of major elements and halogens in WGR samples, obtained by TOF-SIMS, are presented in Supplementary Material Table S3. The aim of TOF-SIMS analysis was to identify the presence of any high Cl-, Br- and I-bearing mineral inclusions. However, no areas of small volume and halogen content above detection limits, indicative of halogen-rich mineral inclusions, were observed in any samples. Additionally, the below-surface depths of halogen-rich fluid inclusions able to be exposed by the ion beam were beyond the profiling depth of TOF-SIMS.

### 5.5. Eclogite Facies Fluid Inclusions

The final melting temperature of ice in samples ranges from −15 to −17 °C, corresponding to salinities between 18.6 and 20.2 wt% NaCl equivalent. The small size of fluid inclusions in mineral samples made microthermometry challenging, and so to

reconstruct the fluid halogen composition we have used the range of calculated NaCl equivalent values. The average NaCl equivalent of samples here is 19.3 wt%, which is broadly consistent with the average salinity (~21.8 wt%) of fluids in previously analysed WGR samples [60].

The halogen content of fluid inclusions (Table 6) has been reconstructed based on the range of Cl content derived from microthermometry and the Br/Cl and I/Cl ratios obtained during NI-NGMS crushing analyses. Reconstructed halogen concentrations are likely to be slight underestimates, as they are based on the assumption that NaCl is the only chloride species, and do not consider other potential chlorides, e.g., KCl and $PbCl_2$. Extensive EDS analyses of several MPIs indicated, however, that concentrations of other chlorides such as KCl are insignificant, and $CaCl_2$, $MgCl_2$, $PbCl_2$ and $FeCl_2$ or other chloride species were not observed in any analyses. The bromine content of fluid inclusions ranges from 868 ppm (QC36A—olivine) to 8938 ppm (QC26C—garnet). Iodine content ranges from 6.4 ppm (QC36Q—quartz) to 169 ppm (QC36A—garnet). These reconstructed halogen concentrations are generally consistent with the Br (500–7300 ppm) and I (1–17 ppm) content of reconstructed fluid inclusions in WGR samples [60]. The average bromine and iodine content of the eclogite facies fluid is ~3000 ppm and ~30 ppm, respectively, which is higher than modern seawater and most crustal rocks and is comparable to a broad range of hydrothermal fluid types (<50 ppm I; [102]), oil and gas field brines and sedimentary formation waters [98,103–105].

**Table 6.** Reconstructed halogen compositions of garnet-hosted fluid inclusions (ppm).

| *Sample* | *NaCl (wt%)* | *Cl* | *Br* | *I* |
|---|---|---|---|---|
| *QC26C-Gt* | 18.6–20.2 | 112823–121441 | 8304–8938 | 21.1–22.7 |
| *QC26E-Gt* | 18.6–20.2 | 112823–121441 | 4264–4590 | 19.7–21.2 |
| *QC26E-Qtz* | 18.6–20.2 | 112823–121441 | 1297–1396 | 6.5–6.9 |
| *QC26G-Gt* | 18.6–20.2 | 112823–121441 | 3328–3582 | 15.5–16.7 |
| *QC26H-Gt* | 18.6–20.2 | 112823–121441 | 2244–2416 | 6.7–7.3 |
| *QC26H-Qtz* | 18.6–20.2 | 112823–121441 | 1636–1761 | 9.7–10.5 |
| *QC36A-Ol* | 18.6–20.2 | 112823–121441 | 868–935 | 17.2–18.5 |
| *QC36A-Gt* | 18.6–20.2 | 112823–121441 | 1421–1530 | 157–169 |
| *QC36D-Gt* | 18.6–20.2 | 112823–121441 | 3249–3497 | 27.4–29.5 |
| *QC36G-Gt* | 18.6–20.2 | 112823–121441 | 3610–3886 | 36.5–39.3 |
| *QC36Q-Qtz* | 18.6–20.2 | 112823–121441 | 1286–1384 | 6.4–6.8 |

A representative Raman spectrum of a garnet-hosted fluid inclusion is shown in Figure 9. Figure 9 shows that the fluid inclusion is dominated by $H_2O$, with the characteristic weak, broad $H_2O$ bending mode observed between Raman shift 1500 and 1600 cm$^{-1}$ and OH stretching modes between Raman shift 3200 and 3700 cm$^{-1}$. The characteristic Raman peaks associated with $CO_2$, $N_2$ and $CH_4$ were not observed during Raman analysis of fluid inclusions. However, this does not preclude the existence of inclusions rich in $CO_2$, $N_2$ and $CH_4$. Fluid inclusions dominated by $H_2O$ are consistent with previously reported fluid compositions in eclogites of the WGR [58].
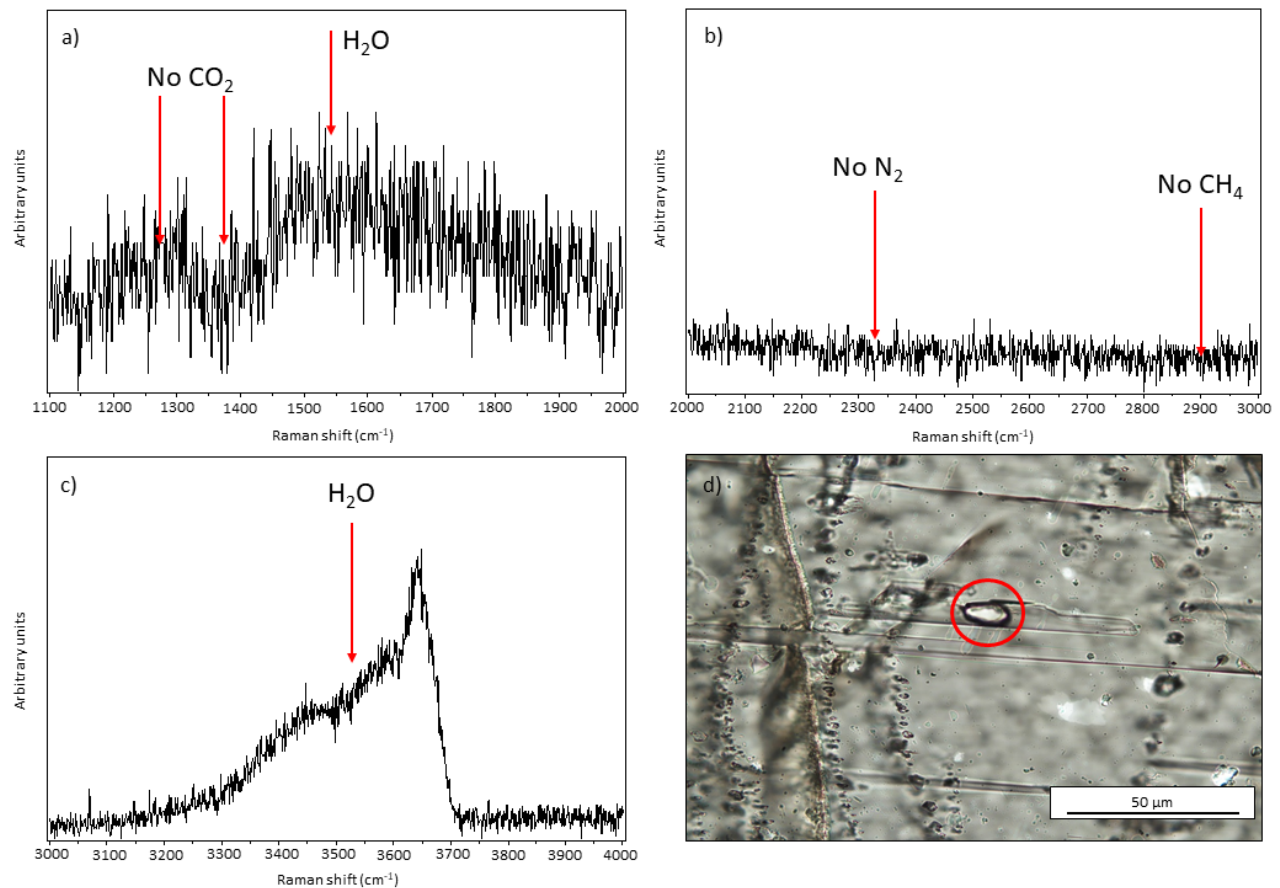
**Figure 9.** Raman spectra of a garnet-hosted fluid inclusion, showing a $H_2O$-rich nature. (**a**) A broad $H_2O$ peak between 1500 and 1600 cm$^{-1}$ and a lack of $CO_2$ peaks between 1300 and 1400 cm$^{-1}$, (**b**) a lack of $N_2$ and $CH_4$ peaks between 2000 and 3000 cm$^{-1}$, (**c**) broad peaks associated with $H_2O$ between 3200 and 3700 cm$^{-1}$, and (**d**) photomicrograph of the analysed fluid inclusion.

## 6. Discussion

### 6.1. Protoliths and Metasomatism

The least metasomatised rock in the Svartberget body is garnet peridotite. Based on its chemical composition and mineralogy, it has been classified as a member of the so-called "Fe-Ti peridotites" that are considered to have been crustal magmatic rocks and were probably intruded into the Fennoscandian craton in the middle or late Proterozoic [55,61,62]. This lithotype is distinctly different from the Mg-Cr-type orogenic peridotites in the WGR that were introduced into the gneisses tectonically, probably from the sub-Laurentian lithospheric mantle. The spectacular vein system with its zoned, websterite-dominated selvages was formed at P-T conditions similar to those pertaining in the upper mantle when the leading edge of the Baltica continental crust was subducted to depths of <100 km below Laurentia. The metasomatic agent was clearly a water-rich granitoid melt or melt-like fluid [63,64]. This locality is significant because the peridotite composition is broadly similar to mantle rocks, so it can act as an analogue for mantle metasomatism. Importantly, the size of the body and scale of the metasomatic features are on a mappable scale, offering an advantage over studies of smaller, fragmented xenoliths. The well-known Mg-Cr class of peridotites in the WGR [44] largely lacks metasomatic products generated under mantle conditions by crust-derived fluids or melts (but see [106] for micro-scale example), so the Fe-Ti class offers us the best case studies in the WGR.

The Årsheimneset mafic-ultramafic body lacks peridotite and is composed of a layered assemblage of metabasic eclogite and various opx-bearing pyroxenites. It may

have been a layered mafic-ultramafic intrusion. The two websterite layers are texturally and compositionally very similar to the metasomatic selvages at Svartberget and to other, similar examples in the Molde area [63] and display mica and garnet-rich veins indicative of an influx of silica and LIL-rich fluid or melt, so a similar origin by metasomatism of an olivine-rich precursor may be inferred. At this locality, the presence of quartz (coesite) eclogite allows comparisons to be made with previously published studies of halogen systematics of other eclogites in the WGR. The vein and depletion halo in this eclogite closely resembles those in eclogites in other subduction systems that have been interpreted as resulting from action of aqueous fluids with a dissolved terrigenous component [80]. The field and petrographic characteristics of the Årsheimneset body are very similar to those in the much larger Eiksunddal massif approximately 40 km to the north [46,75], but Eiksunddal also has layers of Fe-Ti garnet peridotite, which encourages links between Årsheimneset and the Fe-Ti class of peridotites, including Svartberget.

In both bodies, the mineral phases investigated in the present study were clearly generated or modified by metasomatism under UHP conditions, so a major source of the halogens can be directly related to the previously identified, causative metasomatic agent.

### 6.2. Fluid Inclusion vs. Lattice-Bound Halogens

The high proportion of halogens released during crushing analyses—up to 58% Cl, 64% Br and 87% I—the similarity of halogen ratios between crushing and heating analyses (Figure 8), and to previous studies of fluid and brine inclusions [21,60,94], together with the lack of any halogen-rich inclusion phases observed during TOF-SIMS analyses indicate that fluid inclusions dominate the bulk rock halogen compositions. This is consistent with suggestions that at least 80% of bulk rock Cl is hosted in fluid inclusions [107]. The textural relationships of fluid inclusions described previously suggest that they are primary in origin. Therefore, the halogen contents of fluid inclusions in this study offer insight into the halogen systematics of crustal fluids associated with mantle metasomatism during the transient subduction-exhumation of continental crust to UHP conditions.

### 6.3. Fractionation of F and Cl between Minerals and Fluid

Partition coefficients (D) for F/Cl between hydrous mineral phases and fluid can be calculated through: $D = (F/Cl)^{mineral}/(F/Cl)^{fluid}$. It is not possible to measure F abundances with which to derive a fluid F/Cl ratio through NI-NGMS but, given the similarities in salinity and halogen content of fluid between this study and that of previous work [60], it is reasonable to suggest that the fluids have a similar F content. We have, therefore, calculated F/Cl partition coefficients by adopting an average fluid F/Cl value of 0.008 [60], along with EPMA data for minerals in this study. Clinohumite shows the largest mineral-fluid F/Cl partition coefficients (D = 30000); amphibole inclusions show the smallest partition coefficients (D = 38). Amphibole in the matrix and phengite show the same partition coefficients (D = 2500), biotite shows a range in D from 1250 to 3000, and apatite shows a range in D from 625 to 1625; the latter is in good agreement with apatite D values of 900–1100, at 1–2 GPa and 950–1050 °C [108]. Therefore, hydrous minerals are enriched in F, and can be expected to efficiently fractionate F from Cl when crystallising from a fluid. The degree of fractionation is greatest for clinohumite, followed by phengite and amphibole, then biotite and lastly apatite. The growth of clinohumite will thus have the largest impact on the F/Cl ratio of the coexisting fluid. However, since the partition coefficients of the remaining hydrous minerals are largely similar, it is reasonable to suggest that hydrous mineral crystallisation in general will significantly decrease the F/Cl ratio of the coexisting fluid.

### 6.4. Halogen Content of Eclogite Fluids

The halogen compositions of fluids in this study show higher Br/Cl ratios and lower I/Cl ratios than average continental crust and sedimentary formation waters (Figure 8b) and are similar in composition to evaporite-bearing fluids. I/Cl ratios show a similar range to previously analysed Alpine eclogites and garnet peridotites [17,18] but Br/Cl ratios are approximately one order of magnitude higher for an equivalent I/Cl ratio (Figure 8c). Figure 8d shows that the highest Br/Cl ratios of fluids obtained in this study are consistent with previously analysed eclogites from the WGR [60]. They show similar Br/Cl ratios and high halogen concentrations to brine inclusions in mantle-derived diamonds [94] and fluid inclusions in mantle peridotite xenoliths from Siberia [21]. The similarly high Br/Cl, I/Cl and high halogen concentrations between different samples in the sub-continental lithospheric mantle suggest the existence of a common process or end-member source controlling halogen compositions. The elevated Br/Cl ratios seen here are unlikely to result from the addition of Br during dehydration reactions or other subduction-related processes, as there is no known reservoir that is rich enough in Br to cause significant enrichment in mineral phases. It is more likely that the high Br/Cl ratios in fluid here are due to some preferential removal of Cl through, e.g., the formation of micas and other hydrous minerals within the zones of intense metasomatism at the sampled localities. Lower I/Cl ratios here than crustal material and fluids derived from the eclogites of other tectonic regions (Figure 8b) may be explained by the early loss and removal of I from minerals and organic-rich material [97,109,110] during shallower depths of subduction, due to its lower compatibility in silicate phases. Alternatively, the original source of the fluid may have been depleted in I, due to a lack of organic-rich sediments with which to enrich the resulting fluid in I during dehydration reactions as subduction progresses.

### 6.5. Halogen Fractionation through Metamorphic and UHP Metasomatic Processes

Figure 8d shows two trends that depict the halogen evolution of a fluid phase during dehydration and hydration reactions [60]. A residual fluid resulting from the formation of a metamorphic rock via dehydration reactions will have a significantly different halogen composition to a residual fluid resulting from the formation of a metamorphic rock via hydration reactions. During hydration reactions, fluids are subjected to a range of water activities, which allows for the fractionation of incompatible elements into the structure of mineral phases [111]. Thus, as $H_2O$ is consumed during the crystallisation of hydrous mineral phases, Br/Cl ratios will be unchanged until the activity of water in the system ($a H_2O$) is reduced to a level which promotes the crystallisation of Cl-bearing mineral phases, thereby increasing the Br/Cl ratio of the coexisting fluid. The larger ionic radius of $Br^-$, relative to the $OH^-$ ion, prevents significant incorporation of Br within mineral phases. In contrast to hydration reactions, dehydration reactions will result in the release of I from minerals and organic-rich sediments [97,109,110], significantly increasing the I/Cl ratios of the coexisting fluid, e.g., the pore fluid field in Figure 8. Br/Cl ratios are little affected due to the small concentrations of Br in mineral phases, relative to I, with which to enrich the resulting fluid.

The Br/Cl and I/Cl ratios obtained in this study (Figure 8d) are generally consistent with the trend defined by hydration reactions in a previous study of the WGR [60]. The evolution of halogen ratios during hydration reactions also mimics the trend of seawater evaporation [60,112], whereby $a H_2O$ is effectively lowered, without affecting the fluid Br/Cl ratio, until increasing salinity promotes the precipitation of halite, which then drives the Br/Cl and I/Cl ratios of the residual fluid higher. This trend indicates strong fractionation of Cl and Br between minerals and fluids [60]. Thus, the crystallised hydrous phases would be expected to have a significantly lower Br/Cl ratios than the fluid. Using an example of halogen fractionation during halite precipitation, the $(Br/Cl)^{halite}/(Br/Cl)^{solution}$ partition coefficient of 0.032, obtained at room temperature [113], the Br/Cl ratio of the mineral responsible for fractionation is required to be $\sim 8.6 \times 10^{-4}$ [60].

This calculated Br/Cl ratio relies of course on the partition coefficient not changing at high pressure or temperature, which is uncertain. Applying the Br/Cl partition coefficient between halite and solution [113] to samples in this study, the mineral responsible for fractionation would require a Br/Cl ratio ranging between $2.36 \times 10^{-3}$ and $2.46 \times 10^{-4}$, with an average value of $8.12 \times 10^{-4}$, a similar value to that obtained previously [60]. Figure 8c shows that some mica separates in this study have Br/Cl ratios consistent with that required for efficient Cl and Br fractionation. Therefore, micas may be responsible for fractionation of Cl and Br during hydration reactions associated with metasomatism. The paucity of data for I in hydrous mineral phases makes assessing the fractionation of Cl from I difficult. Given the larger ionic radius of I, relative to Br, Cl may be expected to be fractionated from I more strongly than from Br. The low I/Cl ratios in micas and the fractionation trends shown in Figure 8 do, however, appear to trend in the right direction, and suggest that mica may also be responsible for the efficient fractionation of Cl from I.

### 6.6. Halogen Systematics of Fluids in Subducted Crust and Mantle Metasomatism

The halogen composition of the fluid in this study is notably different to halogens retained in the slab during subduction as represented by Alpine eclogites and garnet peridotites [17,18] (Figure 8c). The Alpine eclogites are from ophiolitic complexes and represent subducted oceanic lithosphere and are thus quite different in origin and evolution from the WGR eclogites, whose protoliths resided for a long period as intrusions within continental crust and were subducted along with it.

Taking the two examples described here as models for mantle rocks, and specifically sub-continental lithospheric mantle (SCLM), it is instructive to compare these results with SCLM-derived mantle xenoliths. The SCLM is expected to retain chemical heterogeneities introduced through subduction-related interactions between mantle and crustal sources [114,115] due to its isolated nature and because, unlike the mantle, it does not convect. The SCLM will, therefore, preserve halogens that are released from the slab during subduction and periodically be involved in mantle metasomatism during the ascent of fluids. Fluid inclusions in Siberian mantle xenoliths [21] have high concentrations of halogens, suggesting that that the SCLM can be enriched in volatiles due to metasomatic processes. Their Br/Cl and I/Cl ratios are similar to samples of this study (Figure 8d), while both show significant overlap with the halogen compositions of fluids trapped in minerals of the altered oceanic crust [116]. This suggests that UHP metasomatism of mafic-ultramafic bodies in the WGR and metasomatism in the SCLM could have involved a component derived from seawater.

The sources of eclogitic fluids in the WGR are subject to debate, with suggestions that amphibolite-facies mafic protoliths and the gneissic country rock surrounding mafic-ultramafic bodies are potential origins [58,60,63,64]. Samples in this study show a trend from seawater-like Br/Cl ratios to more Br- and I-rich compositions, generally following a mixing trend defined by seawater and a hypothetical Br- and I-rich endmember (Figure 8c). Most of the samples in this study lie on or close to the mixing line, which indicates that there may have been a seawater component in the metasomatic fluid, but the original seawater was processed and subsequently evolved either during subduction and coeval metasomatism. The process most likely driving the evolution of the seawater is the crystallisation of hydrous mineral phases (though not necessarily just Cl-rich mineral phases) causing the fractionation of halogens via the preferential removal of Cl from Br and I in the fluid.

The fractionation trend in Figure 8d shows that the starting composition of the fluid responsible for metasomatism must have been slightly more I rich than seawater, falling between modern seawater and MORB I/Cl values. Therefore, prior to halogen fractionation, it is likely that the fluid acquired I from I-rich minerals and organic material during the early stages of subduction. Following the addition of I, hydrous mineral crystallisation may have reduced the $a$H$_2$O in the fluid to such an extent that it could, given the large quantities of Cl in seawater, lead to Cl saturation in the residual fluid. A

Cl-saturated fluid will significantly increase mineral-fluid Cl partition coefficients and promote the incorporation of Cl into solid phases [60,111]. The incorporation of Br and I into solid phases is little affected due to the much lower concentration of these halogens in seawater—70 ppm Br and 0.06 ppm I [117]. This notion of Br and I inactivity is consistent with the relatively narrow ranges in Br/I ratios across samples in this study (Figures 7 and S1). The effects of preferential incorporation on the halogen composition can be seen in Figure 8d, where crystallised solid phases will have low Br/Cl and I/Cl ratios, while the residual fluid will evolve to higher Br/Cl and I/Cl ratios. As previously mentioned, micas analysed here have Br/Cl and I/Cl ratios low enough to efficiently fractionate Cl, suggesting that micas may be important in the fractionation of Cl from Br and I.

Mica crystallisation alone is, though, unlikely to account for all of the observed halogen fractionation. It is likely that other Cl-bearing phases such as amphibole or apatite, could fractionate Cl from Br and I during metasomatism. The Br and Cl content of apatites in mantle peridotites [118] give Br/Cl ratios of $0.1–10 \times 10^{-3}$, which is low enough to generate residual fluids with high Br/Cl ratios consistent with those observed in this study and could be a plausible explanation for similar values obtained from brine inclusions in diamonds [94], and in mantle xenoliths from Siberia [21]. It is, therefore, reasonable to suggest that other hydrous phases may also be able to fractionate Cl from Br and I. In the Lindås Nappe (LN) near Bergen, which is a slice of Baltica basement granulite that underwent early Scandian transformation to eclogite, fluid inclusions from quartz veins have up to 30 wt% dissolved salts and no visible water vapour in any inclusions, nor showed any clathrate formation during microthermometry [58]. The authors suggested that water has been selectively removed from the fluid in this region, which is consistent with fractionation and hydration trends suggested here and elsewhere [21,60]. Fluids in the WGR may better represent a more primitive eclogitic fluid than the evolved composition at the Lindås Nappe [58].

Fluid mobility within the WGR is on a much larger scale than in other tectonic settings. For example, in Alpine eclogites, fluid mobility operated on the scale of centimetres, with eclogites acting as closed systems with respect to fluids in the region [119–121]. In contrast, field relations in the Norwegian Caledonides indicate fluid mobility on the scale of metres to kilometres [37,60]. It is, therefore, prudent to consider whether eclogites of the WGR may have acted as open systems with respect to external fluids. An open system allows for the possibility of repeated fluid infiltration and loss from the system, resulting in complex controls on the composition of metasomatic fluids over time. The elevated I/Cl signatures in garnet from sample QC36A (Figure 8) are unlike any other sample in this study and may indicate that more than one fluid composition has interacted this sample, and by implication other UHP eclogites and peridotites of the WGR. The halogen ratios of this garnet suggest that its halogen composition was inherited from pore fluids, and may reflect an early I-rich fluid, which was not modified by further halogen fractionation. The sample is from near the limit of metasomatism in a selvage and may have retained some pre-metasomatic garnet that has retained some earlier fluid. Therefore, multiple fluids of various compositions may have existed and interacted with the Svartberget peridotite. Given that the majority of samples in this study closely follow a trend of apparent fractionation and hydration, it can be assumed that the system appears largely closed, with perhaps a minor component involving external fluid sources.

Numerous saline groundwaters and brines from Precambrian shields have high Br/Cl ratios, similar to samples in this study, and low I/Cl ratios [100,101]. Groundwater and fluid inclusion leachates from the Stripa granite in Sweden also show high Br/Cl ratios [99,102] but have I/Cl ratios similar to samples in this study. These shield and granitic groundwaters have distinctly different halogen signatures to halogen-rich oil field brines and mine waters that have previously been shown to have elevated I/Cl ratios [98,102,103–105], similar to marine pore fluids. The high I/Cl and low Br/Cl ratios of oil field brines, mine and sedimentary formation waters precludes them from being the origin of halogen

signatures in this study. The high Br/Cl ratios in Precambrian shields and granitic groundwaters suggest that the fluid observed here could have originated in these settings. Shield brines have been suggested to form through intense evaporation of seawater, with consequent Cl precipitation and residual Br enrichment, with potential sequestration of I in organic matter before the fluids enter basement material [102,122]. It is suggested further that the Stripa granite halogen composition formed in a similar fashion and represents a modified analog to the Precambrian shield brines [102]. The higher I/Cl ratios in the fluids of the Stripa granite may result from some interaction with organic matter, or limited sequestration of I in organic matter, before entering basement rocks. The process forming these Br-rich groundwaters and brines is, therefore, similar to seawater evaporation and fractionation/hydration trends [60] suggested earlier to explain similar features of the WGR fluids (Figure 8d). The pre-Caledonian evolution of western Baltica is interesting in this regard, because of the extensive marine transgression across the region and deposition of the organic-rich late Cambrian Alum Shale Formation [31]. This shale can be traced well into the WGR [31] and, while it has not been recognised around the two localities under study, it did very likely cover the WGR basement prior to the initiation of Caledonian orogenesis. This offers the possibility of a source of seawater and organic matter, with evaporation during the ensuing regression.

The halogen signatures in this and previous studies of the WGR may, therefore, originate from fluids released during subduction and HP to UHP metamorphism of the continental crust of the Fennoscandian shield and its sedimentary cover. This study adds the contribution of anatexis under UHP conditions, as indicated by the evidence from Svartberget. It has been argued [63] that the UHP conditions make it likely that supercritical fluids were generated by anatexis rather than silicate melts or aqueous fluids, which is supported by the high concentrations of high field strength elements in the metasomatic veins (as seen in the abundant apatite and monazite), a possible result of the strong solvent action of supercritical fluids. The large, combined size of the UHP domain outcrop within the WGR and their correspondence with ultra-coarse, decussate, metasomatic garnet websterites (Figure 1) suggest that subduction of giant UHP terrains might have a significant geochemical influence on the SCLM in collisional orogens, even though subduction was transient. This is reinforced by emerging evidence for earlier, extensive diamond-facies UHP metamorphism in the Seve Nappe Complex of the Scandinavian Caledonides [35] thought to record one or more arc-continent collisions with Baltica during early to middle Ordovician, pre-Scandian closure of Iapetus.

The continental crust is a potential major source of both $H_2O$ and volatiles in the form of sediment and basement pore waters. It is an important alternative fluid and halogen source to the oceanic lithosphere, especially when transient continental subduction episodes occur during arc-continent and continent collisions. Such crust could induce widespread metasomatism of the SCLM during subduction. Overall, despite the equivocal origin of the fluid responsible for metasomatism of the SCLM, the process exerting a controlling factor on the evolution of mantle halogen compositions appears similar for fluid found in different crustal settings: evaporation or hydrous mineral crystallisation induces the precipitation of Cl following a decrease in $a$$H_2O$, which is then followed by a subsequent enrichment in Br and I of the residual fluid. I can also be either inherited from fluid interaction with organic material, or sequestered into organic material early in the subduction process.

The wide range of halogen compositions observed in mantle sources suggests that regions of the mantle are more heterogeneous than previously suggested [21,123]. The range of halogen compositions of the subducting crust [17,18,116] does not match the narrow range in halogen compositions of MORB and OIB source regions [12,14,123]. It has been argued that subduction does not introduce major halogen heterogeneity into the mantle [18]. However, this would require halogens to be decoupled from other volatile species, i.e., nitrogen, oxygen and sulphur that show heterogeneity in the mantle [124]. The high Br/Cl and I/Cl ratios of fluids in this study suggest, by analogy, that the SCLM

may retain a significant quantity of devolatilised Br and I. The Siberian SCLM is enriched in Cl, Br and I by factors of 125, 675 and 100 times, respectively, relative to the depleted MORB mantle (DMM) [21]. The Br- and I-rich nature of such samples of the sub-continental material indicates that the SCLM represents a major halogen reservoir and, therefore, must be considered in future estimates of global volatile budgets and fluxes. The UHP mafic and ultramafic bodies described in this contribution offer a field model for an alternative source (continental crust) and mechanism (metasomatism by partial melts or supercritical fluids) by which halogens may be transferred into the SCLM.

An obvious target for future halogen studies is the Mg-Cr class of orogenic peridotites in the WGR, generally considered to have been entrained from the SCLM [44]. To date, the only published study of metasomatism relating to the Scandian subduction episode in these rocks is from the Bardane body on Fjortoft island, which shows micro-scale veining with similar large-ion-lithophile enriched composition and micro-diamond [106], indicative of a supercritical fluid with a continental or terrigenous sediment source. The veinlets are associated with MPIs bearing solid-phase assemblages similar to Svartberget, including phlogopite, Cl-apatite and diamond [125]. To date, there have been no detailed studies of halogens in these rocks.

## 7. Conclusions

Ultra-high-pressure eclogite facies mafic-ultramafic rocks from two localities in the Western Gneiss Region of the Scandinavian Caledonides, Svartberget and Årsheimneset, contain abundant multi-phase and fluid inclusions within the cores of host crystals. The texture of the MPIs and fluid inclusions indicates that they are primary inclusions formed during the growth of the host mineral. The halogen content of the fluids, therefore, represent the fluid composition at eclogite facies. The fluid composition, reconstructed using microthermometry and halogen ratios obtained by NI-NGMS crushing analyses, contains 11.3–12.1 wt% Cl, 870–8900 ppm Br and 6–169 ppm I. Fluid inclusions show elevated Br/Cl and I/Cl ratios, relative to seawater, indicating Br and I enrichment of the fluid relative to Cl. The evolution of Br/Cl and I/Cl ratios can vary with metamorphic processes such as dehydration (resulting in high I/Cl ratios and low Br/Cl ratios) or hydration (resulting in high Br/Cl ratios and low-to-moderate I/Cl ratios). The high Br/Cl ratios in fluids analysed in this study are likely caused by fractionation of Cl through either hydrous mineral crystallisation or an evaporative process that reduces the $a$H$_2$O in the fluid and promotes the precipitation of Cl as salts, or its incorporation into mineral structures, due to Cl saturation of the fluid. The fractionation of Cl is consistent with the correlation between Br and I in this study, and the lack of correlation between Cl and Br or I. Hydrous mineral phases show F/Cl fractionation in the following order, from greatest to least: clinohumite, phengite, matrix amphibole, biotite, apatite and inclusion amphibole. Previous studies of these rocks [63,64] have identified a granitoid melt, or supercritical fluid, as the geochemical agent responsible for intense metasomatism of the ultramafic rocks and probably mafic eclogite. As the phases analysed here were generated or modified by this metasomatism, this agent would also have been the vector for halogen transport and deposition. Fluids from prior hydration of the protoliths may also have contributed to the fluid source. Ultimately, the halogens could have originated as seawater that has subsequently evolved as saline brines and groundwaters from the surrounding continental crust, further modified during subduction.

The rocks under study here were probably pre-orogenic intrusions into continental crust, but they offer field-based models for metasomatism of the sublithospheric continental mantle. By analogy with these rocks, metasomatism of the SCLM may also be induced by melts or supercritical fluid associated with the transient subduction and UHP metamorphism of continental crust, given its hydrous and volatile-rich nature. The halogen composition of the Svartberget and Årsheimneset bodies is different to the ophiolitic eclogites in the European Alps, possibly because of the continental crustal hosts of the former and oceanic crustal affinities of the latter. The wide range of halogen

compositions observed in mantle-derived material indicates that the mantle is more heterogeneous than previously thought. The SCLM is potentially a major repository for halogens that may significantly influence global volatile fluxes and budgets.

Future studies of subduction-related halogens should focus on the Mg-Cr type, orogenic peridotites of the WGR; their long and complex history [44] may also promise insights into earlier fluid-related activity in the sub-Laurentian SCLM.

**Supplementary Materials:** The following are available online at www.mdpi.com/article/10.3390/min11070760/s1

**Author Contributions:** Conceptualization, A.Q-C, L.H., R.B. and S.C.; methodology, I.L., L.H., L.R.-H., R.B. and R.T.; validation, I.L., L.H., L.R.-H., R.B. and R.T.; formal analysis, L.H. and R.B.; investigation, L.H. and R.B.; resources, L.H.; data curation, L.H.; writing—original draft preparation, L.H., R.B. and S.C.; writing—review and editing, A.P., L.H., R.B. and S.C.; visualization, L.H., R.B. and S.C.; supervision, A.P., G.D., I.L., R.B. and S.C.; project administration, L.H.; funding acquisition, A.P., G.D., I.L., R.B. and S.C. All authors have read and agreed to the published version of the manuscript.

**Funding:** Financial support for this project was provided by NERC grant NE/L002469/1.

**Institutional Review Board Statement:** Not applicable

**Informed Consent Statement:** Not applicable

**Data Availability Statement:** Supporting data can be found online in the Supplementary Materials.

**Acknowledgments:** We thank Steve Stockley for help preparing thin sections and Jon Fellowes for EPMA work. We also thank Vivi Li for handling of the manuscript and two anonymous reviewers for their constructive comments that helped to improve this manuscript.

**Conflicts of Interest:** The authors declare no conflict of interest.

## References

1. Bureau, H.; Foy, E.; Raepsaet, C.; Somogyi, A.; Munsch, P.; Simon, G.; Kubsky, S. Bromine cycle in subduction zones through in situ Br monitoring in diamond anvil cells. *Geochim. Cosmochim. Acta* **2010**, *74*, 3839–3850.
2. Bernini, D.; Wiedenbeck, M.; Dolejs, D.; Keppler, H. Partitioning of halogens between mantle minerals and aqueous fluids: Implications for the fluid flow regime in subduction zones. *Contrib. Mineral. Petrol.* **2013**, *165*, 117–128.
3. Fabbrizio, A.; Stalder, R.; Hametner, K.; Gunther, D. Experimental chlorine partitioning between forsterite, enstatite and aqueous fluid at upper mantle conditions. cells. *Geochim. Cosmochim. Acta* **2013**, *121*, 684–700.
4. Joachim, B.; Pawley, A.; Lyon, I.; Marquardt, K.; Henkel, T.; Clay, P.; Ruzie, L.; Burgess, R.; Ballentine, C.J. Experimental partitioning of F and Cl between olivine, orthopyroxene and silicate melt at Earth's mantle conditions. *Chem. Geol.* **2015**, *416*, 65–78.
5. Bureau, H.; Auzende, A.L.; Marocchi, M.; Raepsaet, C.; Munsch, P.; Testemale, D.; Mezouar, M.; Kubsky, S.; Carriere, M.; Ricolleau, A.; Fiquet, G. Modern and past volcanic degassing of iodine. *Geochim. Cosmochim. Acta* **2016**, *173*, 114–125.
6. Schilling, J.G.; Bergeron, M.B.; Evans, R. Halogens in the mantle beneath the North Atlantic. *Philos. Trans. R. Soc. A* **1980**, *297*, 147–178.
7. Ito, E.; Harris, D.M.; Anderson, T. Alteration of oceanic crust and geologic cycling of chlorine and water. *Geochim. Cosmochim. Acta* **1983**, *47*, 1613–1624.
8. Jambon, A.; Déruelle, B.; Dreibus, G.; Pineau, F. Chlorine and bromine abundance in MORB: the contrasting behavior of the Mid-Atlantic Ridge and East Pacific Rise and implictaions for chlorine geodynamic cycle. *Chem. Geol.* **1995**, *126*, 101–117.
9. Kendrick, M. High precision Cl, Br and I determinations in mineral standards using the noble gas method. *Chem. Geol.* **2012a**, *292–293*, 116–126.
10. Ruzié-Hamilton, L.; Clay, P.; Burgess, R.; Joachim, B.; Ballentine, C.; Turner, G. Determination of halogen abundances in terrestrial and extraterrestrial samples by the analysis of noble gases produced by neutron irradiation. *Chem. Geol.* **2016**, *437*, 77–87.
11. Sumino, H.; Burgess, R.; Mizukami, T.; Wallis, S.; Holland, G.; Ballentine, C. Seawater-derived noble gases and halogens preserved in exhumed mantle wedge peridotite. *Earth Planet. Sci. Lett.* **2010**, *294*, 163–172.
12. Kendrick, M.; Kamenetsky, V.; Phillips, D.; Honda, M. Halogen systematics (Cl, Br, I) in Mid-Ocean Ridge Basalts: A Macquarie Island case study. *Geochim. Cosmochim. Acta* **2012b**, *81*, 82–93.
13. Kendrick, M.; Honda, M.; Pettke, T.; Scambelluri, M.; Phillips, D.; Giuliani, A. Subduction zone fluxes of halogens and noble gases in seafloor and forearc serpentinites. *Earth Planet. Sci. Lett.* **2013**, *365*, 86–96.
14. Kendrick, M.; Jackson, M.; Hauri, E.; Phillips, D. The halogen (F, Cl, Br, I) and $H_2O$ systematics of Samoan lavas: Assimilated-seawater, EM2 and high-$^3He/^4He$ components. *Earth Planet. Sci. Lett.* **2015a**, *410*, 197–209.

15. Kendrick, M.; Honda, M.; Vanko, D. Halogens and noble gases in Mathematician Ridge meta-gabbros, NE Pacific: implications for oceanic hydrothermal root zones and global volatile cycles. *Contrib. Mineral. Petrol.* **2015b**, *170*, 1–20.

16. Kobayashi, M.; Sumino, H.; Nagao, K.; Ishimaru, S.; Arai, S.; Yoshikawa, M.; Kawamoto, T.; Kumagai, Y.; Kobayashi, T.; Burgess, R.; Ballentine, C.J. Slab-derived halogens and noble gases illuminate closed system processes controlling volatile element transport into the mantle wedge. *Earth Planet. Sci. Lett.* **2017**, *457*, 106–116.

17. Hughes, L.; Burgess, R.; Chavrit, D.; Pawley, A.; Tartèse, R.; Droop, G.; Ballentine, C.J.; Lyon, I. Halogen behaviour in subduction zones: Eclogite facies rocks from the Western and Central Alps. *Geochim. Cosmochim. Acta* **2018**, *243*, 1–23.

18. Kendrick, M.; Scambelluri, M.; Hermann, J.; Padrón-Navarta, J.A. Halogens and noble gases in serpentinites and secondary peridotites: Implications for seawater subduction and the origin of mantle neon. *Geochim. Cosmochim. Acta* **2018**, *235*, 285–304.

19. Mei, S.; Kohlstedt, D.L. Influence of water on plastic deformation of olivine aggregates 1. Diffusion creep regime. *Earth Planet. Sci. Lett.* **2000**, *105*, 21457–21469.

20. McGovern, P.J.; Schubert, G. Thermal evolution of the Earth – Effects of volatile exchange between atmosphere and interior. *Earth Planet. Sci. Lett.* **1989**, *96*, 27–37.

21. Broadley, M.W.; Barry, P.H.; Ballentine, C.J.; Taylor, L.A.; Burgess, R. End-Permian extinction amplified by plume-induced release of recycled lithospheric volatiles. *Nat. Geosci.* **2018**, *11*, 682–687.

22. Straub, S.M.; Layne, G.D. The systematics of chlorine, fluorine, and water in Izu arc front volcanic rocks: Implications for volatile recycling in subduction zones. *Geochim. Cosmochim. Acta* **2003**, *67*, 4179–4203.

23. Gee, D.G.; Juhlin, C.; Pascal, C.; Robinson, P. Collisional Orogeny in the Scandinavian Caledonides (COSC). *Geol. fören. Stockh. förh.* **2010**, *132*, 29–44.

24. Stephens, M.B.; Gustavson, M.; Ramberg, I.B.; Zachrisson, E. The Caledonides of central-north Scandinavia—a tectonostratigraphic overview. In *The Caledonide Orogen—Scandinavia and Related Areas*; Gee, D.G., Sturt, B.A., Eds.; Wiley: New York, USA, 1985; pp. 135–162.

25. Stephens, M.B.; Gee, D.G. Terranes and polyphase accretionary history in the Scandinavian Caledonides. In *Terranes in the Circum-Atlantic Paelozoic Orogens*; Dallmeyer, R.D., Ed.; *Geol. Soc. Am. Spec. Pap.* **1989**, *230*, 17–30.

26. Roberts, D. The Scandinavian Caledonides: Event chronology, palaeogeographic settings and likely modern analogues. *Tectonophysics* **2003**, *365*, 283–299.

27. Nordgulen, Ø.; Barnes, C.G.; Yoshinobu, A.S.; Frost, C.; Prestvik, T.; Austrheim, H.; Anderson, H.S.; Marko, W.T.; McArthur, K. Pre-Scandian tectonic and magmatic evolution of the Helgeland Nappe Complex, Uppermost Allochthon. *International Geological Congress*. **2008**, 33 IGC excursion 35, pp. 77

28. Terry, M.P.; Robinson, P. Geometry of eclogite facies structural features: Implications for production and exhumation of UHP and HP rocks, Western Gneiss Region, Norway. *Tectonics* **2004**, *23*, TC2001.

29. Hacker, B.R.; Gans, P.B. Continental collisions and the creation of ultrahigh-pressure terranes: Petrology and thermochronology of nappes in the central Scandinavian Caledonides. *Geol. Soc. Am. Bull* **2005**, *117*, 117–134.

30. Smith, D.C. Coesite in clinopyroxene in the Caledonides and its implication for geodynamics. *Nature* **1984**, *310*, 641–644.

31. Bergstrom, J.; Gee, D.G. The Cambrian in Scandinavia. In *The Caledonide Orogen – Scandinavia and related Areas*; Gee, D.G., Sturt, B.A. Eds.; Wiley: New York, USA, 1985; pp. 247–271.

32. Kylander-Clark, A.R.C.; Hacker, B.R.; Mattinson, J.M. Slow exhumation of UHP terranes: titanite and rutile ages of the Western Gneiss Region, Norway. *Earth Planet. Sci. Lett.* **2008**, *272*, 531–540.

33. Cuthbert, S.J.; Carswell, D.A.; Krogh-Ravna, E.J.; Wain, A. Eclogites and eclogites in the Western Gneiss region, Norwegian Caledonides. *Lithos* **2000**, *52*, 165–195.

34. Robinson, P. Extension of Trollheimen tectonostratigraphic sequence in deep synclines near Molde and Brattvåg, Western Gneiss Region, southern Norway. *Norw. J. Geol.* **1995**, *75*, 181–97.

35. Walczak, K.; Cuthbert, S.; Kooijman, E.; Majka, J.; Smit, M.A. U–Pb zircon age dating of diamond-bearing gneiss from Fjørtoft reveals repeated burial of the Baltoscandian margin during the Caledonian Orogeny. *Geol. Mag.* **2019**, *156*, 1949–1964. https://doi.org/10.1017/S0016756819000268.

36. Hacker, B.R.; Andersen, T.; Johnston, S.; Kylander-Clark, A.R.C.; Peterman, E.M.; Walsh, E.O.; Young, D. High-temperature deformation during continental-margin subduction & exhumation: the ultrahigh-pressure Western Gneiss Region of Norway. *Tectonophysics* **2010**, *480*, 149–171.

37. Jamtveit, B.; Bucher-Nurminen, K.; Austrheim, H. Fluid controlled eclogitization of granulites in deep crustal shear zones, Bergen arcs, western Norway. *Contrib. Mineral. Petrol.* **1990**, *104*, 184–193.

38. Root, D.B.; Hacker, B.R.; Gans, P.B.; Ducea, M.N.; Eide, E.A.; Mosenfelder, J.L. Discrete ultrahigh-pressure domains in the Western Gneiss Region, Norway: implications for formation and exhumation. *J. Metamorph. Geol.* **2005**, *23*, 45–61.

39. Krogh, T.E.; Mysen, B.O.; Davis, G.L. *A Paleozoic age for the primary minerals of a Norwegian eclogite,* Annual Report of the Geophysical Laboratory, Volume 73; Carnegie Institute: WA, USA, 1974; pp. 575–576.

40. Griffin, W.L.; Brueckner, H.K. REE, Rb–Sr and Sm–Nd studies of Norwegian eclogites. *Chem. Geol.* **1985**, *52*, 249–271.

41. Brueckner, H.K. The great eclogite debate of the Western Gneiss Region, Norwegian Caledonides: The in situ crustal *v.* exotic mantle origin controversy. *J. Metamorph. Geol.* **2018**, *36*, 517–527.

42. Robinson, P.; Roberts, D.; Gee, D.G.; Solli, A. A major synmetamorphic Early Devonian thrust and extensional fault system in the mid-Norway Caledonides: relevance to exhumation of HP and UHP rocks. In *New Perspectives on the Caledonides of Scandinavia and Related Areas*; Corfu, F., Gasser, D., Chew, D.M. Eds; Geological Society of London: London, UK, 2014; Special Publication no. 390. pp. 241–270.

43. Young, D.J. Structure of the (ultra)high-pressure Western Gneiss Region, Norway: imbrication during Caledonian continental margin subduction. *Geol. Soc. Am. Bull.* **2018**, *130*, 926–94.

44. Brueckner, H.K.; Carswell, D.A.; Griffin, W.L.; Medaris, L.G.; Van Roermund, H.L.M.; Cuthbert, S.J. The mantle and crustal evolution of two garnet peridotite suites from the Western Gneiss Region, Norwegian Caledonides: an isotopic investigation. *Lithos* **2010**, *117*, 1–19.

45. Austrheim, H.; Corfu, F.; Bryhni, I.; Andersen, T.B. The Proterozoic Hustad igneous complex: a low strain enclave with a key to the history of the Western Gneiss Region of Norway. *Precambrian Res.* **2003**, *120*, 149–175.

46. Jamtveit, B. Metamorphic evolution of the Eiksundal eclogite complex, Western Norway, and some tectonic implications. *Contrib. Mineral. Petrol.* **1987a**, *95*, 82–99.

47. Mørk, M.B.E. A gabbro to eclogite transition on Flemsøy, Sunnmøre, western Norway. *Chem. Geol.* **1985**, *50*, 283–310.

48. Krabbendam, M.; Wain, A. Late-Caledonian structures, differential retrogression and structural position of (ultra)high-pressure rocks in the Nordfjord - Stadlandet area, Western Gneiss Region. *Norges Geologiske Undersøkelse Bulletin* **1997**, *432*, 1, 27–139.

49. Cuthbert, S. Petrology and tectonic setting of relatively low temperature eclogites and related rocks in the Dalsfjord area, Sunnfjord, West Norway. Unpublished PhD Thesis, University of Sheffield, UK, 1985.

50. Cuthbert, S. Exploratory modelling of common crustal rock densities at ambient eclogite facies P-T conditions and some natural examples in a giant UHP terrain: Implications for buoyancy and collision tectonics. Abstract Volume of the 13th International Eclogite Conference. Mattinson, C., Castelli, D., Faryad, S.W., Gilotti, J., Godard, G., Perchuk, A., Rubatto, D., Schertl, H.P., Tsujimori, T., Zheng, Y.F. Eds. 2019 – Petrozavodsk: KRC RAS, 2019; 23; ISBN 978-5-9274-0854-2.

51. Engvik, A.K.; Austrheim, A.; Andersen, T. Structural, mineralogical and petrophysical effects on deep crustal rocks of fluid-limited polymetamorphism, Western Gneiss Region, Norway. *J. Geol. Soc.* **2000**, *157*, 121–134.

52. Wain, A.L.; Waters, D.J.; Austrheim, H. Metastability of granulites and processes of eclogitisation in the UHP region of western Norway. *J. Metamorph. Geol.* **2001**, *19*, 609–625.

53. Krogh, E.J. Metamorphic evolution of Norwegian country-rock eclogites deduced from mineral inclusions and compositional zoning in garnets. *Lithos* **1982**, *15*, 305–321.

54. Konrad-Schmolke, M.; O'Brien, P.J.; de Capitani, C.; Carswell D.A. Garnet growth at high- and ultra-high pressure conditions and the effect of element fractionation on mineral modes and composition. *Lithos* **2008**, *103*, 309–332.

55. Kylander-Clark, A.R.C.; Hacker, B.R.; Johnson, C.M.; Beard, B.L.; Mahlen, N.J.; Lapen, T.J. Coupled Lu–Hf and Sm–Nd geochronology constrains prograde and exhumation histories of high- and ultrahigh-pressure eclogites from western Norway. *Chem. Geol.* **2007**, *242*, 137–154.

56. Andersen, T.; Burke, E.A.J.; Austrheim, H. Nitrogen-bearing, aqueous fluid inclusions in some eclogites from the Western Gneiss Region of the Norwegian Caledonides *Contrib. Mineral. Petrol.* **1989**, *103*, 153–165.

57. Andersen, T.; Austrheim, H.; Burke, E.A.J. Fluid inclusions in granulites and eclogites from the Bergen Arcs, Caledonides of W. Norway. *Mineral. Mag.* **1990**, *54*, 145–158.

58. Andersen, T.; Austrheim, H.; Burke, E.A.J.; Elvevold, S. N$_2$ and CO$_2$ in deep crustal fluids: evidence from the Caledonides of Norway. *Chem. Geol.* **1993**, *8*, 113–132.

59. Svensen, H.; Jamtveit, B.; Yardley, B.W.D.; Engvik, A.K.; Austrheim, H.; Broman, C. Lead and bromine enrichment in eclogite-facies fluids: extreme fractionation during lower-crustal hydration. *Geology* **1999**, *27*, 467–470.

60. Svensen, H.; Jamtiveit, B.; Banks, D.A.; Austrheim, H. Halogen contents of eclogite facies fluid inclusions and minerals: Caledonides, western Norway. *J. Metamorph. Geol.* **2001**, *19*, 165–178.

61. Carswell, D.A.; Harvey, M.A.; Al-Samman, A. The petrogenesis of contrasting Fe-Ti and Mg-Cr garnet peridotite types in the high grade gneiss complex of Western Norway. *Bull. Minéral.* **1983**, 106, 727–750.

62. Reverdatto, V.V.; Selyatitskiy, A.Y.; Carswell, D.A. Geochemical distinctions between "crustal" and mantle-derived peridotites/pyroxenites in high/ultrahigh pressure metamorphic complexes. *Russ. Geol. Geophys.* **2008**, *49*, 73–90.

63. Quas-Cohen, A. Norwegian orthopyroxene eclogites: petrogenesis and implications for metasomatism and crust-mantle interactions during subduction of continental crust. Unpublished PhD thesis. Manchester University, UK, 2014.

64. Vrijmoed, J.C.; Austrheim, H.; John, T.; Hin, R.C.; Corfu, F.; Davies, G.R. Metasomatism in the Ultrahigh-pressure Svartberget Garnet-peridotite (Western Gneiss Region, Norway): Implications for the Transport of Crust-derived Fluids within the Mantle. *J. Petrol.* **2013**, *54*, 1815–1848.

65. Carswell, D.A.; van Roermund, H.L.M.; Wiggers Devries, D.F. Scandian ultrahigh-pressure metamorphismof Proterozoic basement rocks on Fjørtoft and Otrøy, Western Gneiss Region, Norway. *Int. Geol. Rev.* **2006**, *48*, 957–77.

66. Eskola, P. On the eclogites of Norway. *Skr. Vidensk. Selsk. Christiania, Mat-naturv.*, Kl. **1921**, *18*, 1–118.

67. Lappin, M.A.; Smith, D.C. Mantle-equilibrated orthopyroxene eclogite pods from the basal gneisses in the Selje District, Western Norway. *J. Petrol.* **1978**, *19*, 530–584.

68. Lappin, M.A.; Smith, D.C. Carbonate, silicate and fluid relationships in eclogites, Selje district and environs, SW Norway. *Earth Environ Sci Trans R Soc Edinb*, **1981**, *72*, 171–193.

69. Carswell, D.A.; Cuthbert, S.J. Ultrahigh pressure metamorphism in the Western Gneiss Region of Norway. In *Ultrahigh Pressure Metamorphism*; Carswell, D.A., Compagnoni, R. Eds; Budapest, Eotvos University Press. Hungary, 2003, European Mineralogical Union Notes in Mineralogy 5, 51–73.

70. Cuthbert, S.J. Trondhjemite veins in eclogite from the Western Gneiss Region, Norwegian Caledonides; Evidence for partial melting. *Sci. Bull.* **1995**, *40*, 103–104.

71. Labrousse, L.; Jolivent, L.; Agard, P.; Hebert, R.; Andersen, T. Crustal-scale boudinage and migmatization of gneiss during their exhumation in the UHP Province of Western Norway. *Terra Nova* **2002**, *14*, 263–270.

72. Krogh, T.E.; Kamo, S.L.; Robinson, P.; Terry, M.P.; Kwok, K. U-Pb zircon geochronology of eclogites from the Scandian Orogen, northern Western Gneiss Region, Norway:14-20 million years between eclogite crystallization and return to amphibolite-facies conditions. *Can. J. Earth Sci.* **2011**, *48*, 441–47.

73. Mørk M.B.E.; Mearns, E.W. Sm-Nd isotopic systematics of a gabbro-eclogite transition. *Lithos*, **1986**, *19*, 255–267.

74. Beckman, V.; Moller, C.; Soderlund, U.; Corfu, F.; Pallon, J.; Chamberlain, K.R. Metamorphic zircon formation at the transition from gabbro to eclogite in Trollheimen–Surnadalen, Norwegian Caledonides. In *New Perspectives on the Caledonides of Scandinavia and Related Areas*; Corfu, F., Gasser, D., Chew, D. M. Eds; Geological Society, London, UK, 2014, Special Publications, 390, 403–424.

75. Jamtveit, B. Magmatic and metamorphic controls on chemical variations within the Eiksunddal eclogite complex, Sunnmøre, western Norway. *Lithos* **1987b**, *20*, 369–389.

76. Vrijmoed, J.C.; van Roermund, H.L.M.; Davies, G.R. Evidence for diamond-grade ultra-high pressure metamorphism and fluid interaction in the Svartberget Fe-Ti garnet peridotite-websterite body, Western Gneiss Region, Norway. *Mineral. Petrol.* **2006**, *88*, 381–405.

77. Wain, A. New evidence for coesite in eclogite and gneisses: Defining an ultrahigh-pressure province in the Western Gneiss region of Norway. *Geology* **1997**, *25*, 927–930.

78. Vrijmoed, J.C.; Smith, D.C.; Van Roermund, H.L.M. Raman confirmation of microdiamond in the Svartberget Fe–Ti type garnet peridotite, Western Gneiss Region, Western Norway. *Terra Nova* **2008**, *20*, 295–301.

79. Agrinier, P.; Javoy, M.; Smith, D.C.; Pineau. F. Carbon and oxygen isotopes in eclogites, amphibolites, veins and marbles from the Western Gneiss Region, Norway. *Chem. Geol. (Isotope Geoscience Section)* **1985**, *52*, 145–162.

80. Spandler, C.; Hermann, J. High-pressure veins in eclogite from New Caledonia and their significance for fluid migration in subduction zones. *Lithos* **2006**, *89*, 135–153.

81. Griffin, W.L.; Brueckner, H.K. Caledonian Sm-Nd ages and a crustal origin for Norwegian eclogites. *Nature* **1980**, *285*, 319–321.

82. Lappin, M.A.; Pidgeon, R.T.; van Breemen, O. Geochronology of basal gneisses and mangerite syenites of Stadlandet, west Norway. *Nor. J. Geol.* **1979**, *59*, 161–181.

83. Frezzotti, M.L.; Ferrando, S. The chemical behavior of fluids released during deep subduction based on fluid inclusions. *Am. Mineral.* **2015**, *100*, 352–377.

84. Rielli, A.; Tomkins, A.G.; Nebel, O.; Brugger, J.; Etschmann, B.; Paterson, D. Garnet peridotites reveal spatial and temporal changes in the oxidation potential of subduction. *Sci. Rep.* **2018**, *8*, 16411. doi:10.1038/s41598-018-34669-0.

85. Stuart, F.; Turner, G.; Taylor R. He-Ar isotope systematics of fluid inclusions: Resolving mantle and crustal contributions to hydrothermal fluids. In *Noble gas geochemistry and cosmochemistry*; Matsuda, J., Ed.; Terra Scientific Publishing Company: Tokyo, Japan, 1994; pp. 261–277.

86. Henkel T.; Tizard J.; Blagburn D.; Lyon I.C. Interstellar dust laser explorer (IDLE): a new instrument for submicron analyses of stardust — quantification of laser SNMS. *Appl. Surf. Sci.* **2006**, *252*, 7117–7119.

87. Bodnar, R.J. Revised equation and table for determining the freezing point depression of $H_2O$-NaCl solutions. *Geochim. Cosmochim. Acta* **1993**, *57*, 683–684.

88. Deruelle, B.; Dreibus, G.; Jambon, A. Iodine abundances in oceanic basalts: implications for Earth dynamics. *Earth Planet. Sci. Lett.* **1992**, *108*, 217–227.

89. Li, Y. A brief discussion on the mean oceanic residence time of elements. *Geochim. Cosmochim. Acta* **1982**, *46*, 2671–2675.

90. Kastner, M.; Elderfield, H.; Martin, J.B.; Suess, E.; Kvenvolden, K.A.; Garrison, R.E. Diagenesis and interstitial-water chemistry at the Peruvian continental margin — major constituents and strontium isotopes. *In Proceedings for Ocean Drilling Program Scientific Results 112*; Suess, E., von Huene, R., Eds.; College Station: TX, USA, 1990; pp. 413–440. doi:10.2973/odp.proc.sr.112.144.1990.

91. Martin, J.B.; Gieskes, J.M.; Torres, M.; Kastner, M. Bromine and iodine in Peru margin sediments and pore fluids: implications for fluid origins. *Geochim. Cosmochim. Acta* **1993**, *57*, 4377–4389.

92. Fehn, U.; Lu, Z.; Tomaru, H. Data report: [129]I/I ratios and halogen concentrations in pore water of the Hydrate Ridge and their relevance for the origin of gas hydrates: a progress report. 24/32. In *Proceedings for Ocean Drilling Program Scientific Results 204*; Tréhu, A.M., Bohrmann, G., Torres, M.E., Colwell, F.S., Eds.; College Station: TX, USA, 2006; pp. 1–25. doi:10.2973/odp.proc.sr.204.107.2006.

93. Muramatsu, Y.; Doi, T.; Tomaru, H.; Fehn, U.; Takeuchi, R.; Matsumoto, R. Halogen concentrations in pore waters and sediments of the Nankai Trough, Japan: implications for the origin of gas hydrates. *J. Appl. Geochem.* **2007**, *22*, 534–556.

94. Johnson, L.H.; Burgess, R.; Turner, G.; Milledge, H.J.; Harris, J.W. Noble gas and halogen geochemistry of mantle fluids: comparison of African and Canadian diamonds. *Geochim. Cosmochim. Acta* **2000**, *64*, 717–732.

95.   Langmuir, C.; Vocke, R.; Hanson, G.; Hart, S. A general mixing equation with applications to Icelandic basalts. *Earth Planet. Sci. Lett.* **1978**, *37*, 380–392.

96.   Yardley, B.W.D. The evolution of fluids through the metamorphic cycle. In *Fluid Flow and Transport in Rocks; Mechanisms and Effects*; Jamtveit, B., Yardley, B.W.D. Eds.; Chapman & Hall: London, UK, 1997; pp. 99–122.

97.   Wedepohl, K. H. The composition of the continental crust. *Geochim. Cosmochim. Acta* **1995**, *59*, 1217–1232.

98.   Worden, R.H. Controls on halogen concentrations in sedimentary formation waters. *Mineral. Mag.* **1996**, *60*, 259–274.

99.   Nordstrom, D.K.; Lindblom, S; Donahoe, R.J.; Barton, C.C. Fluid inclusions in the Stripa granite and their possible influence on the groundwater chemistry. *Geochim. Cosmochim. Acta* **1989**, *53*, 1741–1755.

100.  Kelly, W.C.; Rye, R.O.; Livnat, A. Saline minewaters of the Keeweenaw Peninsula, northern Michigan: Their nature, origin and relation to similar deep waters in Precambrian crystalline rocks of the Canadian shield. *Am. J. Sci.* **1986**, *286*, 281–308.

101.  Frape, S.K.; Fritz, P. Geochemical trends for groundwaters from the Canadian shield. In *Saline Water and Gases in Crystalline Rocks*; Fritz, P., Frape, S.K. Eds.; Geological Association of Canada Special Paper 33, 1987; pp. 19–38.

102.  Böhlke, J.K.; Irwin, J.J. Laser microprobe analyses of Cl, Br, I, and K in fluid inclusions: implications for sources of salinity in some ancient hydrothermal fluids. *Geochim. Cosmochim. Acta* **1992**, *56*, 203–225.

103.  Olmstead, S.; Muehlenbachs, L.; Shih, J.; Chu, Z.; Krupnick, A.; Shale gas development impacts on surface water quality in Pennsylvania, *Proc. Natl. Acad. Sci. U.S.A.* **2013**, *110*, 4962–4967.

104.  Harkness, J.; Warner, N.R.; Dwyer, G.S.; Mitch, W.; Vengosh, A. Halogens in oil and gas production-associated wastewater. *AGU Fall Meeting* **2014**, H23C-0891 (abstr.).

105.  Harkness, J.S.; Dwyer, G.S.; Warner, N.R.; Parker, K.M.; Mitch, W.A.; Vengosh, A. Iodide, Bromide, and Ammonium in Hydraulic Fracturing and Oil and Gas Wastewaters: Environmental Implications. *Environ. Sci. Technol.* **2015**, *49*, 1955–1963.

106.  Scambelluri, M.; van Roermund, H.L.M.; Pettke, T. Mantle wedge peridotites: Fossil reservoirs of deep subduction zone processes. *Lithos* **2010**, *120*, 186–201, doi:10.1016/j.lithos.2010.03.001.

107.  Urann, B.M.; Le Roux, V.; John, T.; Beaudoin, G.M.; Barnes, J.D. The distribution and abundance of halogens in eclogites: An in situ SIMS perspective of the Raspas Complex (Ecuador). *Am. Mineral.* **2020**, *105*, 307–318.

108.  Brenan, J.M. Partitioning of fluorine and chlorine between apatite and aqueous fluids at high pressure and temperature: implications for the F and Cl content of high P-T fluids. *Earth Planet. Sci. Lett.* **1993**, *117*, 251–263.

109.  Fuge, R.; Johnson, C.C. The geochemistry of iodine – a review. *Environ. Geochem. Health* **1986**, *8*, 31–54.

110.  Muramatsu, Y.; Wedepohl, K. H. The distribution of iodine in the earth's crust. *Chem. Geol.* **1998**, *147*, 201–216.

111.  Sanford, R.F. Mineralogical and chemical effects of hydration reactions and applications to serpentinization. *Am. Mineral.* **1981**, *66*, 290–297.

112.  Worden, R. Halogen elements in sedimentary systems and their evolution during diagenesis. In *The role of halogens in terrestrial and extraterrestrial geochemical processes: surface, crust, and mantle*; Harlov, D.E., Aranovich, L. Eds; Springer: Berlin, Germany, 2018; pp. 185–260.

113.  Fontes, J.; Matray, J.M. Geochemistry and origin of formation brines from the Paris Basin, France: 1. Brines associated with Triassic salts. *Chem. Geol.* **1993**, *109*, 149–175.

114.  Walker, R.; Carlson, R.; Shirey, S.; Boyd, F. Os, Sr, Nd, and Pb isotope systematics of southern African peridotite xenoliths: implications for the chemical evolution of sub-continental mantle. *Geochim. Cosmochim. Acta* **1989**, *53*, 1583–1595.

115.  McDonough, W. Constraints on the composition of the continental lithospheric mantle. *Earth Planet. Sci. Lett.* **1990**, *101*, 1–18.

116.  Chavrit, D.; Burgess, R.; Sumino, H.; Teagle, D.; Droop, G.; Shimizu, A.; Ballentine, C.J. The contribution of the hydrothermal alteration of the ocean crust to the deep halogen and noble gas cycles. *Geochim. Cosmochim. Acta* **2016**, *183*, 106–124.

117.  Li, Y. Distribution patterns of the elements in the ocean: A synthesis *Geochim. Cosmochim. Acta* **1991**, *55*, 3223–3240.

118.  Ionov, D.; Griffin, W.; O'Reilly, S. Volatile-bearing minerals and lithophile trace elements in the upper mantle. *Chem. Geol.* **1997**, *141*, 153–184.

119.  Philippot, P.; van Roermund, H.L.M. Deformation processes in eclogitic rocks: evidence for the rheological delamination of the oceanic crust in deeper levels of subduction zones. *J. Struct. Geol.* **1992**, *14*, 1059–1077.

120.  Selverstone, J.; Franz, G.; Thomas, S.; Getty, S. Fluid variability in 2 GPa eclogites as an indicator of fluid behaviour during subduction. *Contrib. Mineral. Petrol.* **1992**, *112*, 341–357.

121.  Nadeau, S.; Philippot, P.; Pineau, F. Fluid inclusion and mineral isotopic compositions (H-C-O) in eclogitic rocks as tracers of local fluid migration during high-pressure metamorphism. *Earth Planet. Sci. Lett.* **1993**, *114*, 431–448.

122.  Martin, H.; Claeys, P.; Gargaud, M.; Pinti, D.; Selsis, F. 6. Environmental Context. *Earth Moon Planets* **2006**, *98*, 205–245.

123.  Kendrick, M.; Hémond, C.; Kamenetsky, V.S.; Danyushevsky, L.; Devey, C.W.; Rodemann, T.; Jackson, M.G.; Perfit, M.R. Seawater cycled throughout Earth's mantle in partially serpentinized lithosphere. *Nat. Geosci.* **2017**, *10*, 222–228.

124.  Broadley, M.W.; Sumino, H.; Graham, D.; Burgess, R.; Ballentine, C.J. Recycled components in mantle plumes deduced from variations in halogens (Cl, Br, and I), trace elements, and $^3$He/$^4$He along the Hawaiian-Emperor Seamount Chain. *Geochem. Geophys.* **2019**, *20*, 277–294.

125.  Carswell, D.A.; van Roermund, H.L.M. On multi-phase mineral inclusions associated with microdiamond formation in mantle-derived peridotite lens at Bardane on Fjørtoft, west Norway. *Eur. J. Mineral.* **2005**, *17*, 31–42.